Turbulent characteristics and anisotropy in breaking surge waves: A numerical study FREE

Akash Venkateshwaran ; Zhuoran Li ; Shooka Karimpour

Check for updates

View Online   Export Citation

Articles You May Be Interested In

Hydrodynamic shock in Rivers: Physical and numerical modeling of flow structures in tsunami-like bores

Physics of Fluids (October 2023)

Effects of surge and roll motion on a floating tidal turbine using the actuator-line method

Physics of Fluids (July 2023)

Experimental study on flow kinematics of dam-break induced surge impacting onto a vertical wall

Physics of Fluids (February 2023)

Turbulent characteristics and anisotropy in breaking surge waves: A numerical study

View Online   Export Citation   CrossMark

Akash Venkateshwaran,[1] [ID] Zhuoran Li,[2] [ID] and Shooka Karimpour[2,a] [ID]

AFFILIATIONS

[1]Department of Mechanical Engineering, University of British Columbia, Vancouver, British Columbia V6T 1Z4, Canada
[2]Department of Civil Engineering, Lassonde School of Engineering, York University, Toronto, Ontario M3J 1P3, Canada

[a]Author to whom correspondence should be addressed: Shooka.Karimpour@Lassonde.yorku.ca

ABSTRACT

Numerical simulations of breaking weak surge waves produced by the sudden removal of a gate were conducted to investigate turbulent characteristics generated by different mechanisms in the surge front. We conducted numerical studies using Large Eddy Simulation over a range of surge Froude numbers from 1.7 to 2.5, and a wide spectrum of tempo-spatial scales down to the Hinze scale was resolved. We established turbulent statistics by means of Favre-averaging where quantities were weighted by the instantaneous density. Our results demonstrated that the production of turbulent kinetic energy is mainly sourced at the toe, where the shear layer originates. Furthermore, the decomposition of production elements illustrated that the shearing action is the principal driver in the entire surge front. Herein, we also conducted intricate anisotropy analyses, including establishing characteristic shape maps by pointwise eigendecomposition of Reynolds stress tensors. Near the toe at the core of the mixing layer, prolate structures were evident that are mainly stretched in the streamwise direction. Moving from the mixing layer toward the free surface, however, the structure changes to a combination of prolate and oblate features, where the smallest principal stress is nearly in the spanwise direction. In a snapshot, our results illustrate a clear transition in anisotropy from the recirculating region to the mixing layer.

I. INTRODUCTION

Surge waves are flow phenomena that occur due to sudden changes in the flow depth, velocity, or discharge. Such transient flows generate strong mixing, causing severe disruption to ecosystems. Tidal bores, for instance, trigger dramatic pollutant and sediment remobilization and suspension, which drastically affect the water quality.[1] Furthermore, tsunami waves induce debris mobilization and put coastal infrastructures at risk.[2] Based on their analogy with stationary hydraulic jumps,[3] these transient waves are often characterized based on the surge Froude number, Fr_s.

The in-depth mixing in these hydrodynamic shocks is caused by two instability mechanisms: (i) instability initiated at the surge toe due to the sharp velocity gradient, leading to the development of a mixing layer[4] and (ii) instability across the surge front due to phase discontinuity, leading to the formation of a recirculating region in the proximity of the front.[5] In-depth mixing is further confounded by the proximity of these two mechanisms as well as possible interactions with the boundary layer.[6] Capturing the complete dynamics of such transient flow events, from phase discontinuity to various scales of turbulence, remains a challenge both experimentally and numerically. In breaking surge waves of $Fr_s > 1.4$–1.6, the coherent structures near

phase discontinuity are often strong enough to overcome the surface tension, causing entrainment of air which can further be transported and distributed via the mixing region.[7]

In many laboratory experiments on undular ($Fr_s < 1.4$–1.6) and breaking surge waves ($Fr_s > 1.4$–1.6), instruments, such as laser Doppler anemometers and acoustic Doppler velocimeters, are often used which deliver point-based measurements.[5,8] Due to the fixed position of such instruments, the position of the instrument changes in reference to the surge front, and therefore, such methods cannot provide a comprehensive description of turbulent statistics and scales. In addition, many instruments cannot record close to the free-surface.[9] Recently, particle image velocimetry (PIV) has been used to characterize the flow in a stationary hydrodynamic shock.[6,10,11] Other studies also used bubble image velocimetry (BIV) to overcome the limits of applications of PIV to aerated flow and investigate the dynamics of steady breakers considering the air–water interaction.[6]

Using these experimental techniques on turbulent surge waves and hydraulic jumps, there has been significant progress in identifying Reynolds stresses, Turbulent Kinetic Energy (TKE) with its budget terms, and initial insight into flow anisotropy. Mignot and Cienfuegos[12] experimentally investigated the dissipation and

14 November 2024 05:38:19

production of turbulent energy in weak hydraulic jumps, in which they stated most of the production occurred in the vicinity of the shear layer. Wei *et al.*[10] analyzed undular jumps in narrow flumes where they reported on TKE, its production, advection, diffusion, and dissipation. Additionally, they reported an anisotropic feature near the toe and the first crest of the jump. Wüthrich *et al.*[13] described a detailed characterization of strong free-surface turbulence using optical techniques. They provided information on the recurring air–water features and their interplay with TKE. Leng and Chanson[14] experimented on undular and breaking positive surges having Froude numbers in a range of 1.2–2.1. They reported Eulerian time scales, derived from the autocorrelation function; moreover, the integral time and length scales derived from the cross correlation function of velocity fluctuations. The ratio of these scales in different directions indicated the presence of anisotropic characteristics. Chanson and Toi[8] have reported similar observations, using longitudinal and vertical velocity time scales. In hydraulic jumps, Wang and Murzyn[15] investigated the length and time scales of bubbly structures, free-surface structures, and the impingement perimeter in the longitudinal and transverse directions. Longer longitudinal dimensions compared to the transverse direction dimensions were observed in the shear layer, while the opposite was true in the recirculation region. Similarly, Chachereau and Chanson[16] analyzed the length and time scales of free-surface fluctuations in two orthogonal directions for hydraulic jumps having small Froude numbers. They inferred that the free-surface was better correlated for longer distances in the longitudinal direction than in the transverse direction, implying that the turbulence is non-homogeneous and elongated coherent structures encompass the flow in the longitudinal direction.

In addition to the laboratory work, computational studies of two-phase breaking surge waves have recently become more viable through improvements and optimizations in algorithms and computational capacity.[17] Performing numerical studies on this physics, however, remain challenging due to a broad spectrum of time and space scales reported in surge waves and hydraulic jumps, from smaller scale eddies to large dominant horizontal eddies present in the wave front.[18] Among these studies, very few are dedicated to investigating the three-dimensional (3D) hydrodynamic features of coherent structures in breaking waves. This is of particular importance in breaking surge waves where two-dimensional (2D) events, reported in the surge front, rapidly evolve into 3D structures.[19] In breaking hydraulic jumps, Mortazavi *et al.*[7] used Direct Numerical Simulation (DNS) to resolve the Hinze scale and presented data on Reynolds stresses, TKE production and dissipation, spectral analyses, and air entrainment. In breaking waves, Lubin and Glockner[20] implemented Large Eddy Simulation (LES) to study the vortex filaments generated during the early stage of the plunging wave breaking process, while Derakhti and Kirby[21] used LES to study air bubble entrainment, dissipation, and momentum transfer between the two phases.

Thus far, very few studies have been devoted to the detailed turbulent characterization both near the interface and in the mixing layer regions, especially for transient breaking surge waves. Moreover, despite the anisotropic behavior reported in hydraulic jumps and bores, and the co-existence of 2D and 3D coherent structures, quantification of turbulence anisotropy in the wake of surge waves remains a matter of conjecture. By conducting turbulent anisotropy analysis, one gets a complete picture of the turbulent behavior. Such analysis on

Reynolds stress tensor reduces the number of variables by representing them in terms of principal stresses and principal eigenvectors. As a result, anisotropy analysis paints a vivid picture of much information, such as the degree of anisotropy in turbulence, 3D shape of the tensor, and the orientations of turbulent stresses.[22,23]

Hence, the present work was motivated by the need to meticulously investigate the spatial distribution of Reynolds stresses and anisotropy, and their linkage to mixing mechanisms across the surge wave front. With this in mind, we have conducted LES simulations on weak transient breaking surge waves where we have resolved even the smallest Hinze scale in the flow. The surge Froude numbers in this study range from 1.7 to 2.5, where the boundary layer has a minimal interaction with the mixing layer region.[6,17] We assessed anisotropy in Reynolds stress tensor using the Anisotropy Invariant Map (AIM) and characteristic ellipsoids maps. Interconnections between anisotropy and the resolved TKE and production were also explored. The implication of these results on the vivid change in structure from the recirculating region to the mixing region is explained.

This paper has five sections and two appendices, including an introduction and a numerical setup section. In the results, Sec. III, we initially discuss the instantaneous flow features, followed by a discussion on the resolved TKE and its production terms. Subsequently, a comparative study between Favre and Reynolds averaging, and two methods of anisotropy analysis are presented. Next, LES modeling and discretization along with the convergence results and mesh quality are demonstrated in Sec. IV, and brief concluding remarks are provided in Sec. V. Finally, Appendix B provides a careful examination of results against laboratory scale breaking surge waves having a similar Froude range, and Appendix C presents an additional measure to assess the quality of current LES simulations.

II. NUMERICAL SETUP
A. Governing equations

The governing equations are solved using interFoam, an incompressible solver within Open Source Field Operation and Manipulation (OpenFOAM) software. Herein, the Large Eddy Simulation (LES) turbulent model is employed, and the governing equations based on the filtered Navier–Stokes equations are

$$\frac{\partial \rho}{\partial t} + \frac{\partial \rho u_i}{\partial x_i} = 0, \tag{1}$$

$$\frac{\partial \rho u_i}{\partial t} + \frac{\partial \rho u_i u_j}{\partial x_j} = -\frac{\partial p}{\partial x_i} + \mu \frac{\partial^2 u_i}{\partial x_j \partial x_j} + \frac{\partial \tau_{ij}^R}{\partial x_j}. \tag{2}$$

In the above equations, u and p represent the LES resolved velocity and pressure, respectively, where the index notation is used to specify Cartesian coordinates, and ρ is the density. The effect of filtering appears in the residual stress tensor, τ_{ij}^R. The most popular method of accounting for the unresolved residual stresses, τ_{ij}^R, is to use the Boussinesq hypothesis

$$\tau_{ij}^R = \mu_R \left(\frac{\partial u_i}{\partial x_j} + \frac{\partial u_j}{\partial x_i} \right) - \frac{1}{3} \tau_{ii}^R \delta_{ij}, \tag{3}$$

where δ_{ij} is the Kronecker delta, and μ_R represents the residual eddy viscosity which is calculated as

$$\mu_R = \rho C_k \Delta \sqrt{k_R}, \qquad (4)$$

where $C_k = 0.094$, and k_R is the turbulent kinetic energy of the residual motion. The effective filter size, Δ, is calculated using volume in each computational cell, V_{cell}, as $\Delta = (V_{cell})^{1/3}$. Here, we solved the one-equation LES model by Yoshizawa and Horiuti[24] for the subgrid scale turbulent kinetic energy, k_R,

$$\frac{\partial \rho k_R}{\partial t} + \frac{\partial \rho u_i k_R}{\partial x_i} = \frac{\partial}{\partial x_i}\left[(\mu + \mu_R)\frac{\partial k_R}{\partial x_i}\right] - \rho \tau_{ij}^R \varepsilon_{ij} - C_\varepsilon \frac{\rho k_R^{3/2}}{\Delta}, \qquad (5)$$

where $C_\varepsilon = 1.04$. The volume fraction α is introduced to distinguish between the two different phases, where at $\alpha = 1$, the cell is fully occupied with water, and air volume fraction, α_a, is defined as $\alpha_a = 1 - \alpha$. The Volume of Fluid (VOF) method is introduced to capture the two-phase flow, where the governing equation is[25]

$$\frac{\partial \alpha}{\partial t} + \frac{\partial u_i \alpha}{\partial x_i} + \frac{\partial}{\partial x_i}[u_{ci}\alpha(1-\alpha)] = 0. \qquad (6)$$

The third term in Eq. (6) applies the sharpening on the interface artificially,[26] and u_{ci} represents the relative velocity for water and air and is defined as

$$u_{ci} = C_\alpha \frac{|u|}{|\nabla \alpha|}\frac{\partial \alpha}{\partial x_i}, \qquad (7)$$

where C_α is the compression strength with a typical value of 1.[27] The fluid density and dynamic viscosity are calculated using a linear combination of volume fractions

$$\rho = \rho_w \alpha + \rho_a(1-\alpha); \quad \mu = \mu_w \alpha + \mu_a(1-\alpha). \qquad (8)$$

In this study, the continuity, momentum, and phase equations, presented by Eqs. (1), (2), and (6), respectively, are standard LES governing equations derived by introducing spatial filtering to incompressible and constant density flow conditions. In this approach, the subgrid convective term appears in the filtered equations that require modeling. However, applying the filter to a flow of variable density, in this case, two-phase flow, introduces additional subgrid unsteady and viscous terms in the momentum equation, and an additional interfacial transport term in Eq. (6) due to the two-phase nature of the flow.[28,29] For oil–water gravity-driven mixing, Vincent et al.[29] demonstrated that the convective term remains dominant through all mixing phases. They included the surface tension term in their study, and the subgrid surface tension term was reported to be significant in areas of decreasing inertia. Furthermore, they reported that the effect of the interfacial transport term is not negligible. It has also been demonstrated by others[28,30,31] that the effect of surface tension is predominant in low shear regions and should be investigated when the density and viscosity difference between the two fluids is small. This indicates the importance of density-varied LES modeling, especially when focusing on near interface dynamics, and even more so when resolving flow features in smaller than the Hinze scale. The present study deals with the air–water interactions (high density difference) in surge waves driven by shearing phenomenon, and although turbulent statistics are discussed in the entire surge front, attention is mainly drawn to the toe region. Therefore, the LES model is considered for the closure of only the convective term. As a result, only the resolved flow quantities participate in the air entrainment and bubble formation, while the role of the subgrid flow quantities, such as subgrid surface tension and interface curvature, is neglected.

B. Computational setup and parameters

Figure 1 demonstrates an instantaneous snapshot of the simulation problem, where U_1 is the uniform downstream flow velocity, and d_1 is the initial downstream water depth. Similarly, U_2 and d_2 denote the uniform velocity and water depth upstream of the breaking surge wave, respectively. As discussed later, the initial condition resembles a dam-break wave setup where $U_1 = 0$. Therefore, in this study, surge wave Froude number, Fr_s, can be determined by

$$Fr_s = \frac{c}{\sqrt{gd_1}}, \qquad (9)$$

where c is the celerity of the wave. In this work, we have considered three surge Froude numbers: $Fr_s = 1.71, 2.13$, and 2.49. The lowest surge Froude number in our study represents the highest Froude number threshold reported for undular surge waves.[5,32] Another dimensionless parameter relevant to surge waves and similar phenomena, such as hydraulic jumps, is the Weber number, which is defined as $We = \rho_q U_2^2 h/\sigma$. Using d_1, the Weber number in the current study ranges from $We \approx 8900$ to 9450. At this range, the contribution of surface tension to energy balance is negligible as reported by Iafrati[33] and Chen et al.[34]

The initial conditions for these breaking surge waves are generated based on analytical equations presented in the literature using the Method of Characteristics (MOC).[35] Initial water level in the reservoir was set to $d_0 = 1\,\mathrm{m}$. The computational domain stretches from

Gate at $t = 0$ s

c

Surge toe

d_2 U_2 Shear layer U_1 d_1
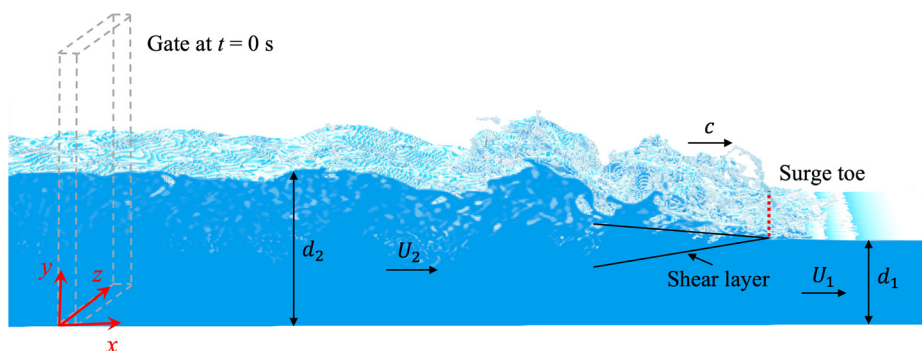
y z x

FIG. 1. Definition sketch of the positive surge wave.

$x = -25$ to 25 m, where $x = 0$ m marks the separation of d_0 and d_1, demarcated by a gate at $t = 0$ s in Fig. 1. The streamwise size of the computational domain is selected so that the negative and positive characteristics do not reach the physical boundaries upstream and downstream during the simulation period of 8 s. We have implemented a periodic boundary condition in the spanwise z-direction.[36,37] This spatial periodic boundary condition is implemented to reintroduce the velocities in the spanwise direction into the flow field.[36] The size of the periodic domain width, $T = 0.4$ m, is selected so that it is several times larger than the largest flow scale in the domain as reported by Li et al.[17] Here, δ is representative of the local grid size across the domain, and in each simulation, the domain is resolved using three different local grid sizes: $\delta = \delta x_1 = \delta y_1 = \delta z_1$ covering the area of wave propagation in the Area of Refinement 1 (AR1); and $\delta = \delta x_2 = \delta y_2 = \delta z_2$ covering the toe where the mixing layer is originated in the Area of Refinement 2 (AR2). The rest of the domain is discretized with a mesh size of $\delta = \Delta x = \Delta y = \Delta z$. Using this grid size combination, we resolved scales down to the Hinze scale (see Appendix A) and have maintained LES resolution throughout the domain, as discussed in Sec. IV. There is no special treatment conducted for the no-slip boundary condition near the bed nor is the grid refined near the rigid boundary. In weak breaking surge waves, as demonstrated by Lin et al.[6] for hydraulic jumps, the interaction of the boundary layer and the mixing layer is limited to areas upstream of the surge wave. In the present study, the effect of the boundary layer region is not captured, first as we only focused on the surge toe and the breaking front with limited interaction with the boundary layer; and second, as the Froude number is limited to 2.49 where our initial water depth, d_1, is significantly larger than the boundary layer thickness.[7] Table I summarizes the parameters for five simulation cases and Froude numbers, where the upstream uniform velocity and depth, U_2 and d_2, are estimated based on MOC. The computing times for cases 1, 2–2, and 3 were 28–35 days, with 128 cores, and for cases 2–3 were roughly 3 months, for a simulated time of 8 s.

The temporal discretization is semi-implicit, and we have employed different spatial discretization schemes for the convection terms. The convection terms appear in momentum, k_R transport, as well as the phase equation, and spatial discretizations are performed based on the sensitivity and nature of these terms as discussed below. The discretization of the subgrid scale turbulent kinetic energy flux, k_R, appearing in Eq. (5), is performed using a first-order upwind biased interpolation. However, the advection flux in the momentum equation requires higher order approximation, and, therefore, an upwind biased central differencing is selected. As demonstrated in Fig. 1, starting from its initial condition, the moving surge wave exhibits discontinuity

in phase at the surge front, and it requires a TVD scheme, or an alternative, to ensure numerical stability and accuracy.[4,27] For the phase flux term in Eq. (6), the VanLeer Total Variation Diminishing (TVD) method is selected. This TVD scheme is second order accurate and is bounded, and its accuracy can drop to as low as first order in regions with discontinuity. Gauss linear central differencing is implemented for diffusive terms, and time marching is conducted using the backward Euler method. The pressure–velocity coupling in the Navier–Stokes equations is conducted using the PISO algorithm.

III. RESULTS AND DISCUSSION

Analysis and discussion of the results are undertaken in several steps. First, to demonstrate the general behavior of a breaking surge wave, instantaneous flow features are qualitatively discussed. This is followed by an in-depth discussion of the turbulent kinetic energy production and mechanisms that mainly contribute to production. To establish the anisotropic characteristics of the flow, anisotropy maps and shapes are established for Froude numbers of $Fr_s = 1.71$, 2.13, and 2.49. Anisotropy is then discussed in terms of relation to instability mechanisms and the production of the resolved turbulent kinetic energy.

A. Instantaneous flow and general observations

Here, we start with a qualitative visualization of the flow. To identify the vortices and their evolution behind the surge wave in space and time, we have used the Q-criterion, where Q is the second invariant of the velocity gradient tensor

$$Q = \frac{1}{2}(||\Omega|| - ||\varepsilon||), \tag{10}$$

where the strain rate is defined as $\varepsilon_{ij} = \frac{1}{2}(\partial u_i/\partial x_j + \partial u_j/\partial x_i)$, and vorticity is defined as $\Omega_{ij} = \frac{1}{2}(\partial u_i/\partial x_j - \partial u_j/\partial x_i)$. There are two distinguishable regions across the surge front: the shear or the mixing layer and the recirculating or the roller region near the air–water interface. Identification of these two regions using the characteristic shapes of turbulence is discussed later in this paper. The toe of the surge is the origin of the shear mixing layer, forming as two different streamwise velocities intersect. Subsequently, the surge toe becomes a source of air entrainment and vortices as seen in Fig. 2. The propagating wave front interacts with the downstream static flow causing the upward movement of the free-surface and rolling action which leads to perturbation of the surface. As a consequence, this causes rolling and recurring actions that, in turn, create a foamy region at the air–water interface.[38] Turbulent vortices and air pockets are advected upstream in the developing shear mixing layer. This region is chaotic and constantly

TABLE I. Summary of parameters for numerical cases. d_2, U_2, and c are obtained using MOC. Grid refinement studies are performed for cases 2–1, 2–2, and 2–3 for Fr_s = 2.13 with a refinement ratio of $r = 1.25$.

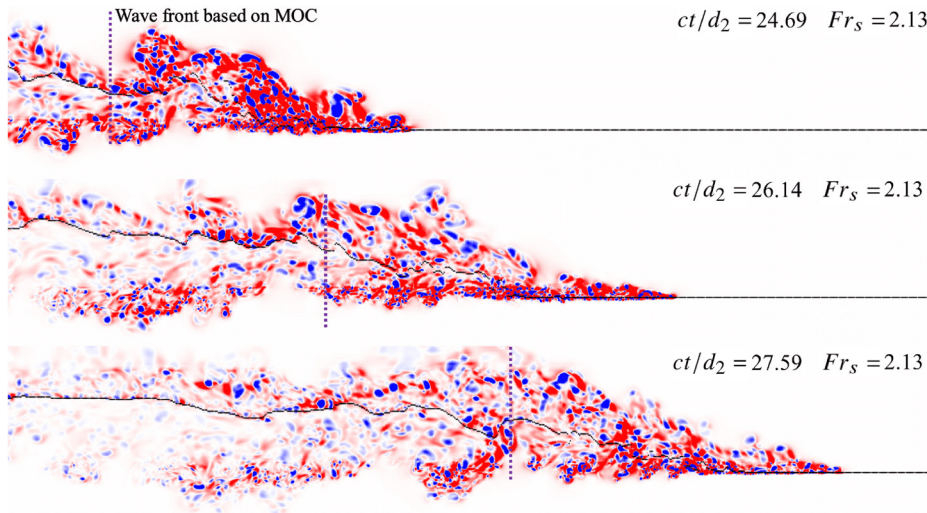| Case nos.	Fr_s	d_1 (m)	d_2 (m)	U_2 (m/s)	c (m/s)	AR1 (m^2)	δx_1 (m)	AR2 (m^2)	δx_2 (m)	Δx (m)
1	1.71	0.300	0.596	1.457	2.93	25 × 0.7	0.00500	10 × 0.1	0.002500	0.0100
2–1	2.13	0.200	0.513	1.820	2.98	25 × 0.6	0.00625	10 × 0.1	0.003125	0.0125
2–2	2.13	0.200	0.513	1.820	2.98	25 × 0.6	0.00500	10 × 0.1	0.002500	0.0100
2–3	2.13	0.200	0.513	1.820	2.98	25 × 0.6	0.00400	10 × 0.1	0.002000	0.0080
3	2.49	0.150	0.461	2.037	3.02	25 × 0.5	0.00500	10 × 0.1	0.002500	0.0100

FIG. 2. Time evolution of the Q-criterion at the mixing layer and the breaking front for $Fr_s = 2.13$ across the channel centerline. The black curve corresponds to $\alpha = 0.5$, identified as the air–water interface.

changing in shape as the wave propagates. Furthermore, as shown in Fig. 2, despite these mixing processes, the wave celerity obtained by MOC represents well the overall propagation of the wave.

Figure 3 demonstrates the side view of the breaking surge wave having $Fr_s = 2.13$ propagating from the left to the right, while the temporal and spatial propagations of the surge wave are normalized using MOC celerity, as seen in Table I. The evolution of the volume fraction of water using three temporal instances is shown in the left column, and the corresponding evolution of coherent vortical structures, using the Q-criterion plots, is shown in the adjacent column. The transient surge is made stationary using a weighted algorithm presented in our previous study.[17] The surge front is shifted to the initial position by subtracting the distance traveled, which is calculated using a theoretically estimated celerity of the wave based on its Froude

number. The mean air–water interface is delineated herein after by $\alpha = 0.5$, also used by Mortazavi et al.[7] and Ling et al.[39]

Statistical averaging in Secs. III B–V is conducted over 400 (frequency of 200 Hz) time steps after the flow has reached a statistically steady turbulent condition. For the current simulation, this has approximately occurred at $ct/d_2 = 20$ for $Fr_s = 1.71$ to $ct/d_2 = 26$ for $Fr_s = 2.49$. In order to determine that the turbulence characteristics are time invariant, we have conducted ensemble averaging over multiple sets of 400 time steps, with a lag time of 0.5 s, and determined the corresponding averaged velocities and Reynolds stresses, as described in Subsection III B. The ensemble quantities conduced for sets starting at or after the above-mentioned statistically steady times were time invariant. The pointwise differences between the averaged velocities among these sets along the x and y directions were limited to
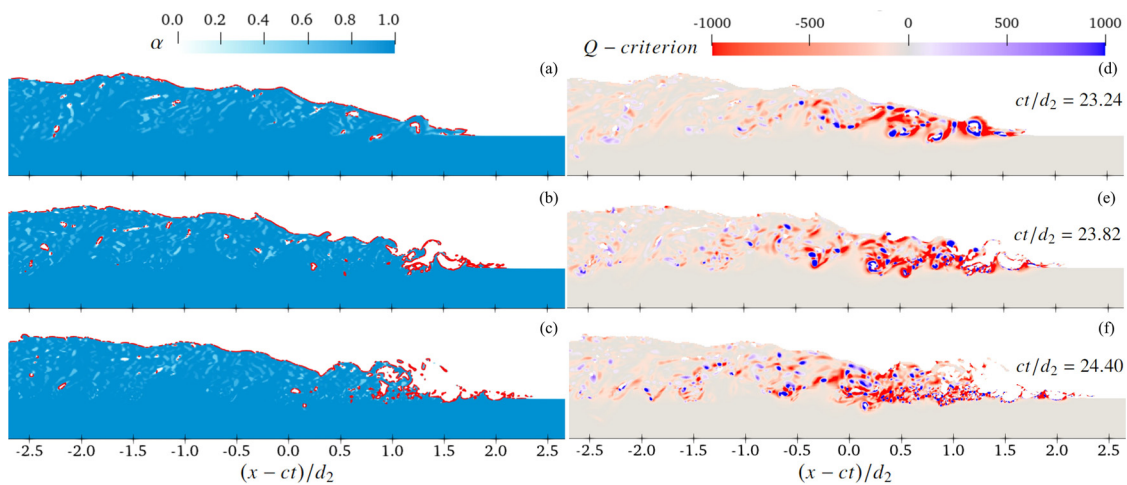

FIG. 3. Shifted instantaneous wave profiles at the centerline for (a)–(c) water volume fraction, α, and (d)–(f) Q-criterion at $Fr_s = 2.13$ for $ct/d_2 = 23.24$, 23.82, and 24.40 below the interface at $\alpha = 0.5$.

$0.005 U_2$. Similarly, the absolute pointwise differences between normal Reynolds stresses were below $1.000 \times 10^{-3} U_2^2$.

B. Resolved turbulent kinetic energy equation

To characterize turbulence across surge waves, here we look from the energy point of view. In the Reynolds decomposition of the flow field, the averaging of the quantities is conducted both temporally and spatially in the z-direction. In the current study, due to the transient nature of the flow, for temporal averaging, time-shifting is also performed using wave celerity c, to normalize the wave position in the streamwise, x-direction. The details of this procedure are provided in Li *et al.*[17] The time and space averaging is defined as

$$\bar{\phi}(x,y) = \frac{1}{n_t n_z} \sum_t \sum_T \phi(x - ct, y, z), \qquad (11)$$

where $n_t = 400$, and in cases 1, 2–2, and 3, $n_z = 40$. Here, we use $\overline{()}$ to denote ensemble average conducted over time using combined spanwise and shifted frames, while the perturbations from this mean are defined as $\phi' = \phi - \bar{\phi}$. In the present problem, there is a significant temporal and spatial change in phase distribution. In the current VOF approach, the density of each phase remains constant; however, the combined phase density in a computational cell, ρ, changes with time and space. As a result, Favre averaging, that is density-weighted averaging, is employed to account for density variation. The Favre averaging operator is defined as

$$\widetilde{\phi} = \frac{\overline{\rho\phi}}{\bar{\rho}}, \qquad (12)$$

and the resolved fluctuations are expressed as $\phi'' = \phi - \widetilde{\phi}$. Further comparisons and reasons to implement Favre averaging are substantiated in Sec. III D. Based on the momentum governing equation for the LES, the transport equation for the resolved turbulent kinetic energy, k, is given by

$$\frac{\partial \bar{\rho} k}{\partial t} = 0 = \underbrace{-\frac{\partial \bar{\rho} \widetilde{u}_j k}{\partial x_j}}_{(1)} \underbrace{-\bar{\rho}\widetilde{u_i'' u_j''}\frac{\partial \widetilde{u}_i}{\partial x_j}}_{(2)} \underbrace{-\overline{\tau_{ij}\frac{\partial u_i''}{\partial x_j}}}_{(3)} + \underbrace{\overline{p'\frac{\partial u_i''}{\partial x_i}} - \overline{u_i''}\frac{\partial \bar{p}}{\partial x_i}}_{(4)}$$
$$+ \underbrace{\frac{\partial}{\partial x_j}\left[\overline{\tau_{ij} u_i''} - \frac{1}{2}\overline{\rho u_j'' u_i'' u_i''} - \overline{p' \rho u_j''}\right]}_{(5)} + \underbrace{\overline{\frac{\partial u_i'' \tau_{ij}^R}{\partial x_j}} - \overline{\tau_{ij}^R \frac{\partial u_i''}{\partial x_j}}}_{(6)}, \qquad (13)$$

where the resolved turbulent kinetic energy is the trace of Reynolds stress tensor, which is defined as $k = \widetilde{u_i'' u_i''}/2$. Term (1) in Equation 13 is the advection term, while (2) is the resolved turbulent production. Term (3) is dissipation due to the effect of molecular viscous stress, τ_{ij}, defined as

$$\tau_{ij} = \mu\left[\frac{\partial u_i}{\partial x_j} + \frac{\partial u_j}{\partial x_i} - \frac{2}{3}\delta_{ij}\frac{\partial u_i}{\partial x_i}\right]. \qquad (14)$$

Term (4) is composed of pressure dilation and pressure gradient, whereas (5) is the diffusion term. Since ensemble averaging in the present problem is conducted over time and space, the resolved turbulent

kinetic energy is time-independent of the left hand side of the equation. Term (6) appears in the Favre-averaged turbulent kinetic energy equation due to the existence of the residual stress in the LES equations. This term includes the transfer of energy between the resolved and subgrid scale as well as subgrid diffusion of the resolved kinetic energy.[40] From the calculation that will be discussed later, the resolved turbulent kinetic energy comprises more than 90% in a small region near the surge toe, and more than 95% elsewhere in the domain. The contribution of term (6) is deemed negligible in the current problem and setup. Similar equations for turbulent kinetic energy, excluding term (6), have been also presented by Mortazavi *et al.*[7] and Ling *et al.*[39] and before them by Aupoix *et al.*[41]

C. Turbulent production and its decomposition

This section is devoted to the production of the turbulent kinetic energy and its predominant role in anisotropy. To assess the role of turbulent production on perturbation growth, the total production, S, is decomposed into three terms, S_1, S_2, and S_3, which are associated with the production of $\widetilde{u'' u''}$, $\widetilde{v'' v''}$, and $\widetilde{w'' w''}$, respectively. These production terms are defined as

$$S_1 = -\widetilde{u'' u_j''}\frac{\partial \widetilde{u}}{\partial x_j}; \quad S_2 = -\widetilde{v'' u_j''}\frac{\partial \widetilde{v}}{\partial x_j}; \quad S_3 = -\widetilde{w'' u_j''}\frac{\partial \widetilde{w}}{\partial x_j}. \qquad (15)$$

In our assessment of the flow field, the spanwise mean velocity, and its spatial derivatives in the x- and y-directions, $\partial \widetilde{w}/\partial x$ and $\partial \widetilde{w}/\partial y$, are negligible. Furthermore, since shifted time averaging combined with spatial spanwise averaging as shown in Eq. (11) are applied, all mean velocity components are invariant in the z-direction, i.e., $\partial \widetilde{u}_i/\partial z = 0$. Subsequently, the production of S_3 also becomes negligible, compared to S_1 and S_2, as seen in Fig. 4.

From Fig. 4, it is evident that the production terms contributing to $\widetilde{u'' u''}$, that is S_1, are dominant in all three Froude numbers. The contour distribution of this production term, shown in the first row, is mainly distributed around the mixing layer originated from the surge toe. S_2 term, shown in the second row in Fig. 4, has the second highest contribution to production. The distribution of S_2 appears to extend mainly behind the breaking surge front and in a shallower depth compared to S_1. This term also exhibits an interesting feature, that is negative turbulent production, mainly at the averaged air–water interface, instantaneously identified at $\alpha = 0.5$.

Figure 5 shows the two components of S_i for $Fr_s = 2.13$, which are S_{ia} and S_{ib}. From the inspection of the contour of S_{1a}, which is $-\widetilde{u'' u''}\frac{\partial \widetilde{u}}{\partial x}$, we observe a negative TKE production below the water surface at the core of the mixing layer, as shown in Fig. 5(a). This indicates the draining mechanism of energy from a fluctuating component to the mean flow. This behavior is consistent throughout the mixing layer which is initiated from the surge toe. Since this term is comprised of the streamwise normal Reynolds stress, which is always positive, the negative TKE production occurs because $\frac{\partial \widetilde{u}}{\partial x} > 0$. This can be physically associated with the stretching of the mean flow in the streamwise direction. The remaining S_1 production term S_{1b}, $-\widetilde{u'' v''}\frac{\partial \widetilde{u}}{\partial y}$ is generated by the Reynolds shear stress $-\widetilde{u'' v''}$, as shown in Fig. 5(b). Across the mixing layer and underneath the breaking surge, S_{1b} is dominant over S_{1a}, and subsequently, the contour for S_1 in Fig. 4(e) closely resembles that of S_{1b}. To compare the magnitude of Reynolds stresses,
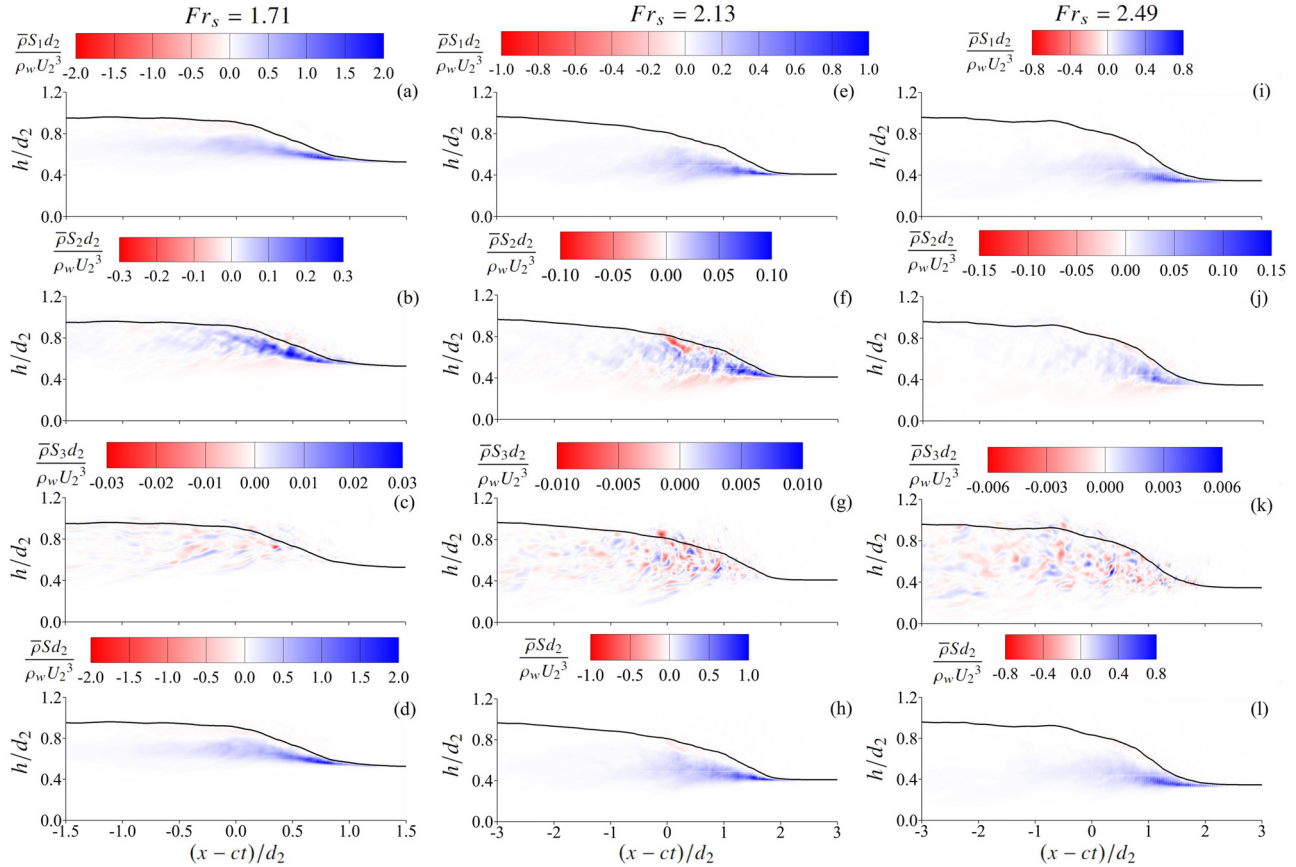
FIG. 4. Normalized TKE production terms, S_1, S_2, and S_3, and total production, S, Froude numbers of $Fr_s = 1.71$, plotted in (a)–(d), $Fr_s = 2.13$, plotted in (e)–(h), and for $Fr_s = 2.49$, shown in (i)–(l), respectively. The black curve corresponds to the averaged air–water interface, instantaneously identified at $\alpha = 0.5$.

normalized $\widetilde{u''u''}$, $\widetilde{v''v''}$, and $-\widetilde{u''v''}$ contours plots are shown in Fig. 6 for $Fr_s = 2.13$. Among the three stresses plotted in this figure, $\widetilde{u''u''}$ is dominant, while the shear stress $-\widetilde{u''v''}$ is smaller in overall distribution. This indicates that the velocity gradient of $\frac{\partial \tilde{u}}{\partial y}$ is the main driver behind the S_{1b}, hence, S_1 production terms as well. Therefore, the gradient of velocity, due to the formation of the mixing layer originated at the surge toe, is the principal driver of high production behind the breaking surge waves studied here.

The next production term S_{2a}, which is $-\widetilde{v''v''}\frac{\partial \tilde{v}}{\partial y}$, is also shown in Fig. 5(c). In this case, we observe the opposite behavior compared to S_{1a} from Fig. 5(a). The production term is spread across the exact region as S_{1a} with an opposite sign. Across the mixing layer, this production is positive because $\frac{\partial \tilde{v}}{\partial y}$ is suspected to be negative, which is characterized by compression of the mean flow in the y-direction. This is expected because the density variation below the interface and across the mixing layer is not dominant as shown in Fig. 3, i.e., $\frac{\partial \tilde{v}}{\partial y} \simeq -\frac{\partial \tilde{u}}{\partial x}$. This also conveys the stretching of the mean flow in one direction leads to compression in the orthogonal direction. Thus, at

the vicinity of the toe, there is an elongation of the mean flow in the flow direction from S_{1a}, whereas compression occurs in the perpendicular direction from S_{2a}. This investigation is further extended using anisotropy maps and ellipsoids in Secs. III E and III F. The remaining production term S_{2b}, which is $-\widetilde{u''v''}\frac{\partial \tilde{v}}{\partial x}$, does not contribute significantly to S_2, as the velocity gradient of $\frac{\partial \tilde{v}}{\partial x}$ is small.

Figure 5 also illustrates the presence of both positive and negative TKE production which implies the source and drain of turbulent energy, respectively. The gradient of velocity due to the formation of the mixing layer originated at the surge toe, $\frac{\partial \tilde{u}}{\partial y}$, is the principal driver of high production behind the breaking surge waves studied here. Therefore, the dominant positive production term, S_1, is observed within the surge at the shear mixing layer. On the contrary, negative values occur close to the surface, which is evident in both S_1 and S_2. This is perhaps due to the formation of negative shear stress, $-\widetilde{u''v''} < 0$, near the interface. Additionally, the positive TKE production in the order of magnitude is substantially larger than the negative. This is in agreement with the results reported by Misra et al.[42] in an experimental study on a weak hydraulic jump. They found positive
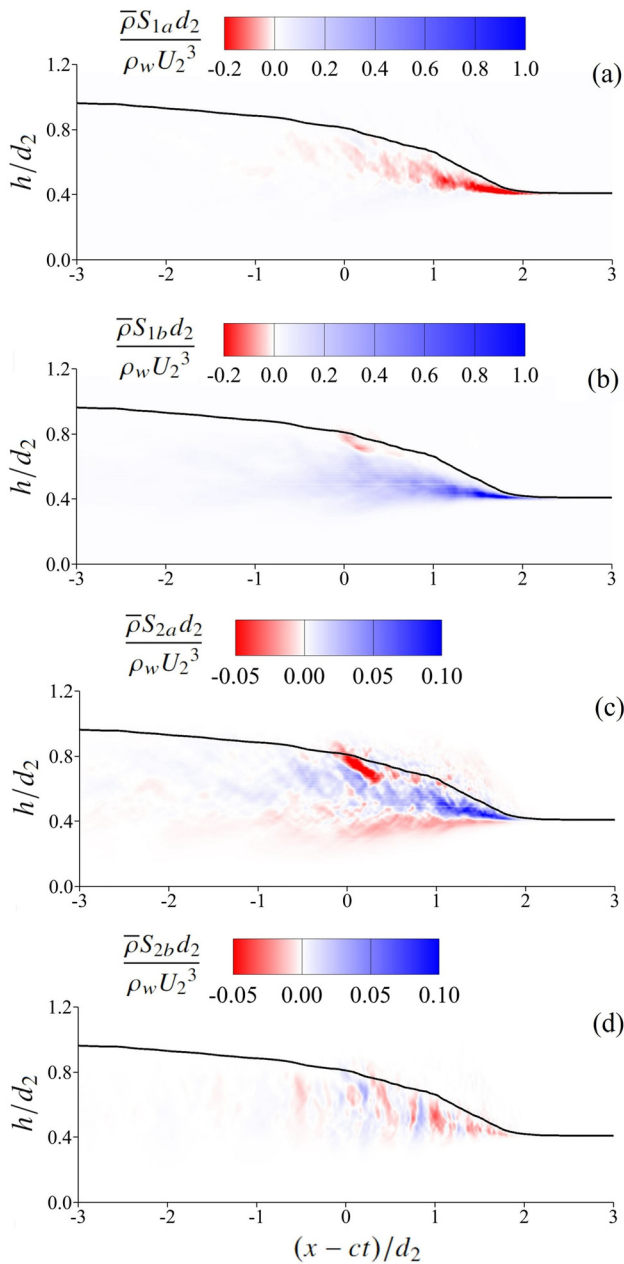
FIG. 5. Resolved Favre-averaged TKE production terms. Components of S_1: (a) S_{1a} and (b) S_{1b}; components of S_2: (c) S_{2a} and (d) S_{2b} based on Eq. (15) for $Fr_s = 2.13$.

Reynolds shear stress in the mixing layer and negative stress just below the mean surface of the hydraulic jump. They also observed high TKE in the mixing layer compared to the surface. This is also supported by a numerical study by Wei *et al.*,[10] who presented observations of negative production of TKE near the free-surface of the first crest in the undular hydraulic jump.
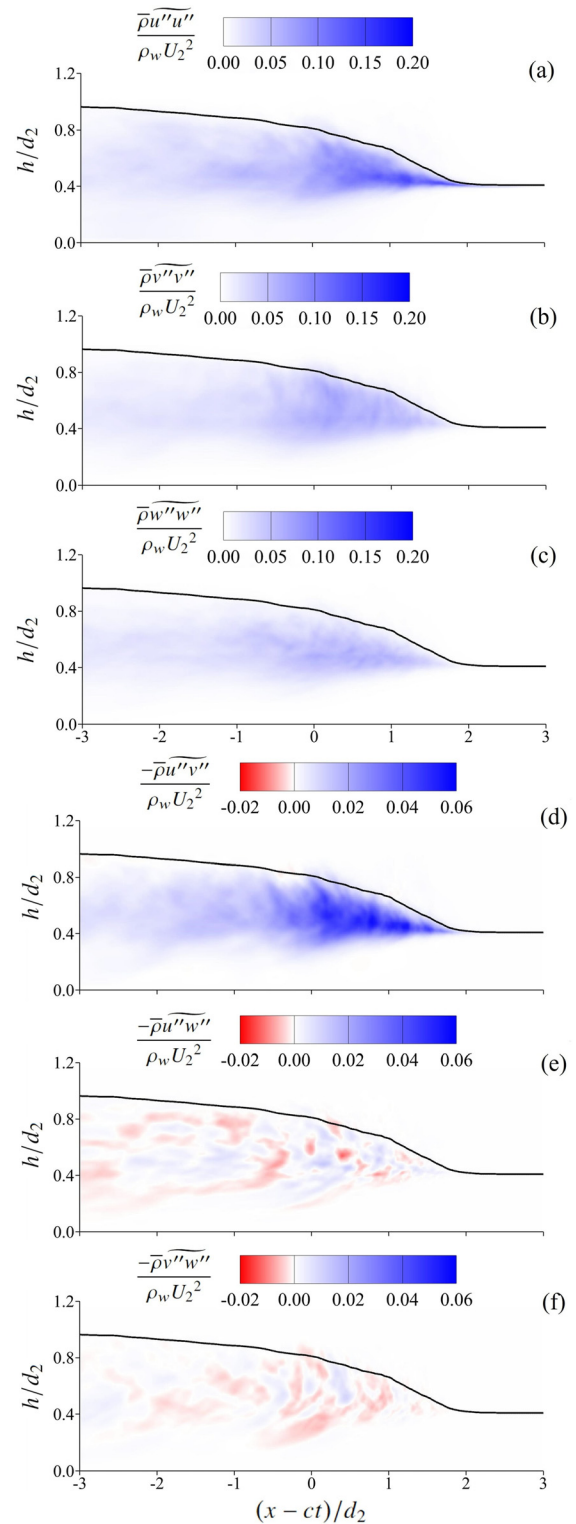

FIG. 6. Favre-averaged normalized turbulent stress terms (a) $\widetilde{u''u''}$, (b) $\widetilde{v''v''}$, (c) $\widetilde{w''w''}$, (d) $-\widetilde{u''v''}$, (e) $-\widetilde{u''w''}$, and (f) $-\widetilde{v''w''}$ for $Fr_s = 2.13$.

D. Favre vs Reynolds averaging

While Reynolds averaging has been widely used in the experimental and computational research conducted on bores, surge waves, and hydraulic jumps, limited attention has been drawn to the impact of density variability on this averaging technique. In the present problem, we deal with an incompressible two-phase flow where the density of each phase remains constant, but there are temporal fluctuations in density at a given location, especially in the vicinity of the mixing layer and the surface interface (see Fig. 3). Thus, when considering this variable-density flow, Favre averaging, density-weighted averaging,[43] or density-varied Reynolds averaging must be employed. This subsection presents a comparison between two averaging techniques: Favre-averaging and constant density Reynolds averaging to discuss the shortcomings of this Reynolds averaging technique for surge waves.

A one-to-one comparison between the two averaging methods on the Reynolds stress components and the total production of the resolved TKE is illustrated in Fig. 7. TKE production terms according to Favre averaging is from Eq. (15) and constant density Reynolds-averaging are as follows:

$$S_r = -\overline{u'u'_j}\frac{\partial \overline{u}}{\partial x_j} - \overline{v'u'_j}\frac{\partial \overline{v}}{\partial x_j} - \overline{w'u'_j}\frac{\partial \overline{w}}{\partial x_j}. \qquad (16)$$

The dissimilarity between the two is confined to the mixing layer and the surface of the water due to high-density fluctuations in those regions. Particularly, anomalies that are observed in normal stress components, close to the toe, in the Reynolds averaging do not exist in Favre averaging. Moreover, the shear Reynolds stress exhibits negative values in the vicinity of the toe at the air–water interface, which is not observed in Favre-averaged shear stress. In terms of the total production, negative production, indicated by the blue color, at the surface of the toe is also of less intensity in the Favre averaging. However, the negative production from $(x - ct)/d_2 = 0$ to 1 still persists for both methods.

It is critical to note that Favre and Reynolds averaging represent two different physical flow kinematics. Following the definitions of Reynolds and Favre averaging, we have

$$\widetilde{u_i} = \frac{\overline{(\bar{\rho} + \rho')(\overline{u_i} + u'_i)}}{\bar{\rho}} = \overline{u_i} + \frac{\overline{\rho'u'_i}}{\bar{\rho}}. \qquad (17)$$

It can also be shown that $\widetilde{u_i} = \overline{u_i} - \overline{u''_i}$. Therefore, the difference between the averaged velocities using these two techniques is the turbulent mass flux term, $\overline{\rho'u'_i}/\bar{\rho}$, which can also be represented by $\overline{u''_i}$. In the Reynolds averaging framework for density varied flow, the turbulent mass flux term appears in the continuity, momentum, and production terms of the TKE equation. As shown by Hendrickson and Yue,[44] in the wave-breaking region in ship wakes, the turbulent mass flux's contributions to the mean momentum equation are of the same magnitude as the Reynolds stress terms. As shown in Fig. 8, all three components of the mass flux term, presented by $\overline{u''}$, $\overline{v''}$, and $\overline{w''}$, are prominent in areas near the interface and the toe region. While the contour plots of $\overline{v''}$ and $\overline{w''}$ show a mixture of positive and negative values across the entire surge front, $\overline{u''}$ demonstrates consistently negative values near the interface and positive values at the mixing layer. The existence of these mass flux terms in the varied density Reynolds

averaging framework can explain the difference between the two averaging methods. Therefore, if a Reynolds averaging framework is implemented in breaking surge waves, bores, and hydraulic jumps, the terms directly associated with the variable density turbulent flows must be incorporated.[45]

E. Anisotropy invariant maps

To investigate the anisotropic behavior of turbulence across a surge wave, here we implement AIM. The anisotropic characteristics of turbulence can first be quantified using the properties of normalized Reynolds stress anisotropy tensor

$$a_{ij} = \frac{\widetilde{u''_i u''_j}}{2k} - \frac{1}{3}\delta_{ij}, \qquad (18)$$

where δ_{ij} is the Kronecker delta. Eigen decomposition of a_{ij} yields three eigenvalues (λ_1, λ_2, and λ_3) and are associated with eigenvectors ($\vec{v_1}$, $\vec{v_2}$, $\vec{v_3}$) which, in turn, are used to calculate the invariants of the tensor.

The Anisotropy-Invariant Map (AIM) introduced by Lumley and Newman[46] is an effective visualization tool to study the states of turbulence and its dynamics by examining the trajectories of the invariants. The coordinates in AIMs are calculated either by linear or non-linear combinations of their corresponding eigenvalues. Among common AIMs are the Lumley triangle, Turbulence triangle, and Barycentric Map (BM). The non-linear Lumley and Turbulence triangles provide distorted representation and visual bias of turbulent quantities. The points on these maps are concentrated, which leads to bias and the trajectories of points are non-linear in nature. On the other hand, BM compensates for these limitations because it linearizes the Reynolds stress tensor.[23] The limiting states of turbulence (one-component, two-component, and three-component) in the BM are evenly spaced in the Euclidean space which prevents the bias. These states are placed at $(x_{1c}, y_{1c}) = (1, 0)$, $(x_{2c}, y_{2c}) = (0, 0)$, and $(x_{3c}, y_{3c}) = (1/2, \sqrt{3}/2)$, to form an equilateral triangle. Any state of turbulence representing a point (x_B, y_B) on the BM is defined by a convex combination of these limiting state vertices

$$\begin{aligned} x_B &= C_{1c}x_{1c} + C_{2c}x_{2c} + C_{3c}x_{3c}, \\ y_B &= C_{1c}y_{1c} + C_{2c}y_{2c} + C_{3c}y_{3c}, \end{aligned} \qquad (19)$$

and the scalar metrics are

$$\begin{aligned} C_{1c} &= \lambda_1 - \lambda_2, \\ C_{2c} &= 2(\lambda_2 - \lambda_3), \\ C_{3c} &= 3\lambda_3 + 1. \end{aligned} \qquad (20)$$

In order to better visualize the anisotropy using the BM, here we use the visualization technique proposed by Emory and Iaccarino,[22] where BM color maps can be directly projected into the physical domain to comprehend the turbulent structures and their dimensions. This is a more convenient technique as it prevents sophisticated labeling and provides the leverage of mapping every point of the physical domain to the BM using colors. In this study, two color maps are used, i.e., the conventional RGB and modified RGB. The conventional RGB values are calculated using the scalar metrics according to the following equation:
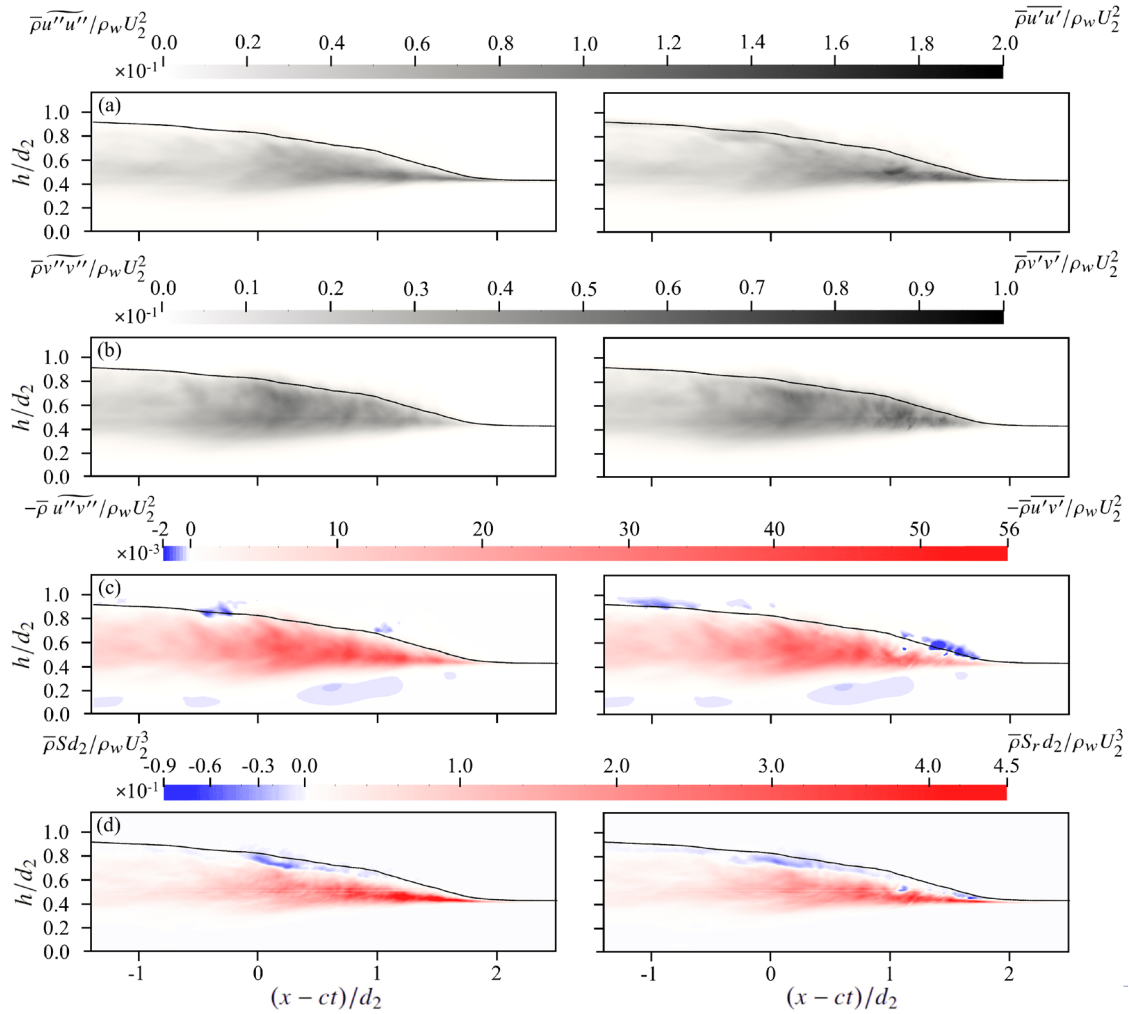
FIG. 7. Comparison of turbulent characteristics obtained from Favre (left column) and Reynolds averaging (right column): (a) $\bar{\rho}\widetilde{u''u''}/\rho_w U_2^2$ vs $\overline{\rho u'u'}/\rho_w U_2^2$, (b) $10\delta x_1$ vs $\bar{\rho}\widetilde{v''v''}/\rho_w U_2^2$, (c) $-\widetilde{v''w''}$ vs $-\overline{\rho u'v'}/\rho_w U_2^2$, and (d) $\bar{\rho}Sd_2/\rho_w U_2^3$ vs $\bar{\rho}S_r d_2/\rho_w U_2^3$.

$$
\begin{bmatrix} R \\ G \\ B \end{bmatrix} = C_{1c} \begin{bmatrix} 1 \\ 0 \\ 0 \end{bmatrix} + C_{2c} \begin{bmatrix} 0 \\ 1 \\ 0 \end{bmatrix} + C_{3c} \begin{bmatrix} 0 \\ 0 \\ 1 \end{bmatrix}. \tag{21}
$$

The modified RGB color scheme provides better distinguishable regions on the BM using more colors by introducing offset (C_{off}) and exponent coefficients (C_{exp}) in Eq. (21). The modified equation for this color scheme is

$$
\begin{bmatrix} R \\ G \\ B \end{bmatrix} = C_{1c}^* \begin{bmatrix} 1 \\ 0 \\ 0 \end{bmatrix} + C_{2c}^* \begin{bmatrix} 0 \\ 1 \\ 0 \end{bmatrix} + C_{3c}^* \begin{bmatrix} 0 \\ 0 \\ 1 \end{bmatrix}, \tag{22}
$$

where $C_{ic}^* = (C_{ic} + C_{\text{off}})^{C_{\text{exp}}}$, $C_{\text{off}} = 0.65$, and $C_{\text{exp}} = 5$. The modified AIM color scheme brings a new perspective, as it further divides the BM into multiple regimes (illustrated in Fig. 9), which aids in

interpreting the intermediate states of turbulence in the complex flow. In particular, distinct colors are assigned to regimes in between the limiting states of turbulent. For example, the axis-symmetric prolate (between one- and three-component) state is assigned a pink color, whereas the cyan indicates the oblate state (between two- and three-component). The conventional and modified BM color maps are shown in Fig. 10 for different Froude numbers.

The first prominent feature is the formation of a clear and distinctive thin layer of one-component turbulence emanating from the toe of the surge front, which can be seen in Figs. 10(a1), 10(b1), and 10(c1) for $Fr_s = 1.71$, 2.13, and 2.49, respectively. This anisotropic turbulent behavior begins at the shear mixing zone under the surge front where the high-speed surge is in immediate contiguity to the stagnant water. This causes the adverse velocity gradient that is believed to be responsible for the production of turbulence and induction of shear stress into the flow. As a result, the increase in TKE and
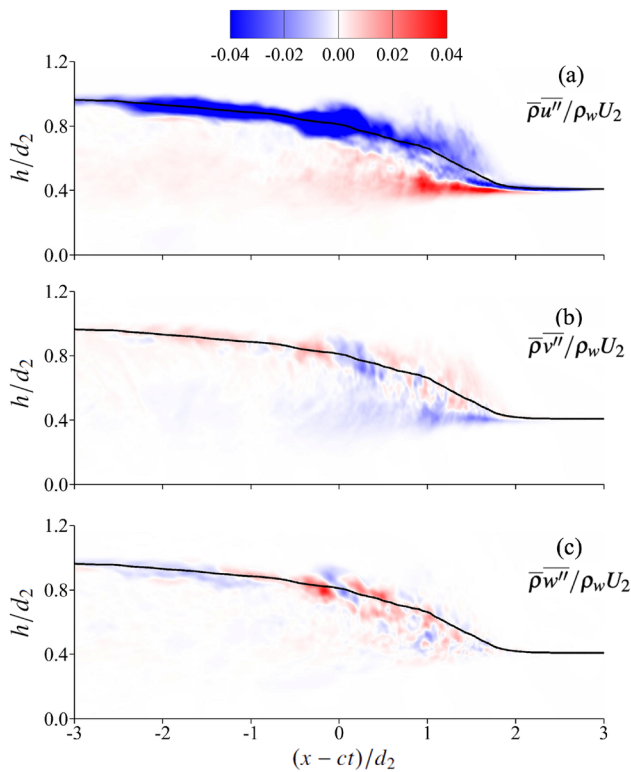
FIG. 8. Plots of (a) $\overline{\rho\,u''}/\rho_w U_2$, (b) $\overline{\rho\,v''}/\rho_w U_2$, and (c) $\overline{\rho\,w''}/\rho_w U_2$ for $Fr_s = 2.13$. These contour plots present turbulent mass flux terms.

its production helps sustain that state of anisotropy behind the surge front. Another salient feature of Fig. 10(b1) is the blue patches, occasionally combined with green for the area behind the surge heel at $(x - ct)/d_2 < 0$. This indicates the three-dimensional isotropic turbulence and the return to the isotropic state behind the surge. As the turbulent kinetic energy cascades from large eddies to small eddies, and eventually, dissipates, the anisotropy decreases; subsequently, the turbulence field almost becomes homogeneous and three-dimensional.

Using the modified color map, Figs. 10(a2), 10(b2), and 10(c2) describe the dominance of prolate characteristics of turbulence across the air–water interface between the surge heel and the toe. The red one-dimensional turbulence at the surge toe seen in the previous discussion transforms into a three-dimensional elongated state as other components of turbulence gain comparable magnitudes. This escalation of the pink color grade follows the pattern of the mixing layer and spreads as the distance from the surge toe increases. Further upstream beyond $(x - ct)/d_2 < 0$, we begin to see highlights of the blue color grade, which suggests the beginning of the return-to-isotropy. Similar observations were made by Nadaoka et al.[47] for breaking waves in the surf zone, where rather two-dimensional flow structures close to the wave crest were reported. However, as described by Nadaoka et al.[47] in such a flow, turbulent structure evolves quickly into that with strong three-dimensionality behind the wave. In Figs. 10(a2) and 10(c2), highlights of blue shapes having a mixture of oblate and isotropic ellipsoids begin to appear at $(x - ct)/d_2 = -1$ and $(x - ct)/d_2 = 0.5$ in the case of $Fr_s = 1.71$ and $Fr_s = 2.49$, respectively, implying that the

return-to-isotropy is faster and closer to the surge front for higher Froude numbers.

The modified color map has all six color distinctions intersecting at the center of the BM as in Fig. 9(b). Thus, the turbulent states near the center of the BM are inconsistent with the color scheme because a minor shift in their position can cause significant color alternation and so does its delineation. Due to this limitation of the color map, intermixing of the pink and cyan colors is noticeable in Figs. 10(a2), 10(b2), and 10(c2), especially in the upstream region of the surge and the top region of the recirculation region. Therefore, these regions have neither entirely prolate nor oblate shapes but rather a blend of the two. These turbulent structures in the form of ellipsoids are illustrated in Sec. III F.

The last feature to report here, which is consistent for all the cases, is the presence of one-dimensional characteristics in the downstream region of the surge front. It may seem sensible that the turbulence should be isotropic at this region as the water is at rest, but we observed this behavior due to the normalization of Reynolds stress tensor with TKE. The TKE and Reynolds stresses are near zero in this region, and, therefore, upon normalization with such low quantities, the tensor obtained is indefinite and yields such a highly anisotropic attribute.

The findings from these analyses are in fundamental agreement with the experimental and statistical studies in breaking bores reported by Chanson and Toi[8] and Leng and Chanson.[14] They observed a large streamwise auto-correlation length scale and timescale compared to the transverse and spanwise directions, which clearly demonstrates an anisotropic process. Moreover, Koch and Chanson[48] and Chanson and Docherty[49] performed turbulent measurements by investigating the Reynolds stresses in undular and breaking bores. They reported large normal and tangential Reynolds stresses beneath the surge which were inhomogeneous and anisotropic in nature. Apart from this, an examination of turbulent intensities through a series of experiments for different Froude numbers on hydraulic jumps in a narrow flume by Wei et al.[10] revealed anisotropic intensities at the jump toe and gradually returned to isotropy upstream. These previously described features are evident and consistent in all three Froude numbers.

F. Characteristics shapes of turbulence

The characteristic shapes of turbulence or the ellipsoids delineate the directionality of turbulence. In Sec. III E, the color maps described the degree of anisotropy and the type of anisotropic structures based on turbulence dimensionality at every location on the domain. Here, the ellipsoids complete the picture by describing the orientation associated with each principal component derived from its eigenvector. These ellipsoids are acquired by the diagonalization of a Reynolds stress tensor. This matrix is diagonalized to get the magnitude of principal stresses (σ_1, σ_2, and σ_3), which are the eigenvalues of the tensor, while the unit vectors that correspond to the direction of principal stresses are its eigenvectors. Once the three principal stresses are obtained for every data point, the corresponding turbulence spheroid for each data point can be acquired from the following equation:

$$\left(\frac{x'}{\sigma_1}\right)^2 + \left(\frac{y'}{\sigma_2}\right)^2 + \left(\frac{z'}{\sigma_3}\right)^2 = 1, \tag{23}$$
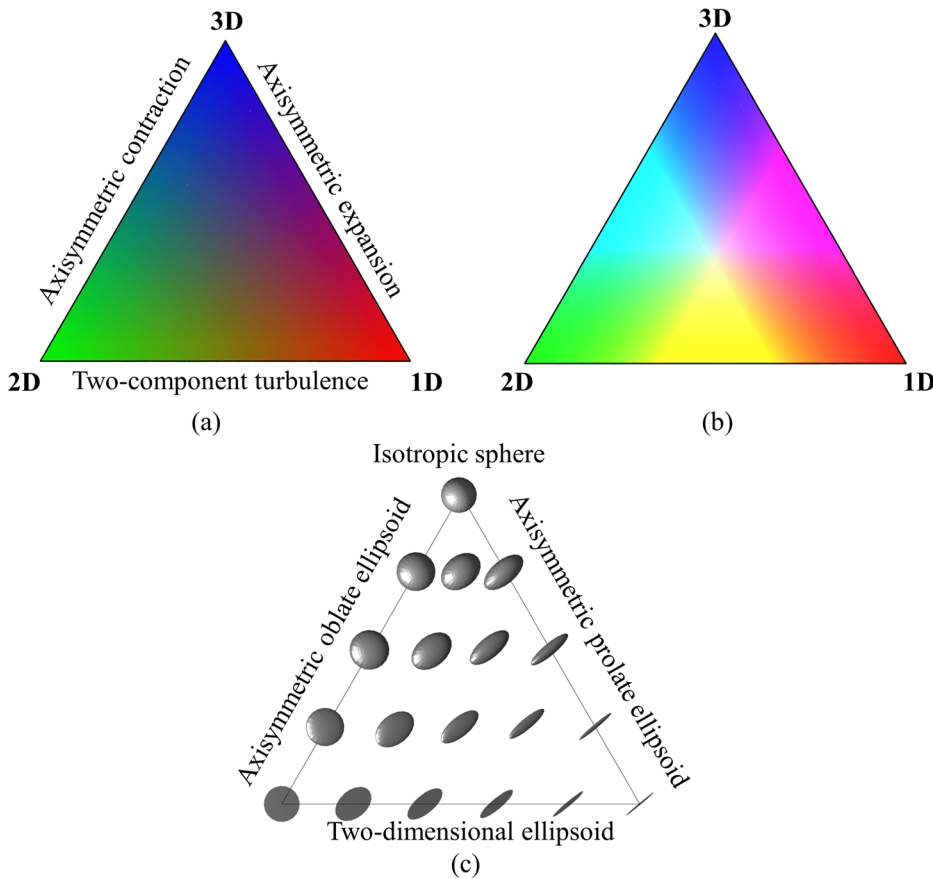
FIG. 9. (a) The conventional and (b) the modified color map representation based on BM; (c) spheroid visualization across the BM.

where x', y', and z' are in the principal coordinate system, while σ_1, σ_2, and σ_3 are the lengths of the semi axes of the turbulence spheroid.

In a special case, when all the principal stresses are equal, the shape obtained is a sphere indicating isotropic property. An oblate spheroid is produced when one of the principal components or an eigenvalue is small compared to the other two; in contrast, a prolate spheroid is produced when an eigenvalue is prevalent compared to the other two eigenvalues. These shapes are illustrated in Fig. 9(c) along with the BM color maps. Once the ellipsoid is composed of Eq. (23), its orientation is rotated such that its semi-axes coincide with these principal axes. In order to demonstrate the orientation of the spheroids in the domain, a color scheme is designed and assigned to three eigenvectors. Figure 11(a) shows the color convention used to visualize these eigenvectors and associated principal stresses: green is assigned to the largest principal stress, red to intermediate, and blue to the smallest principal stress.

Figure 12 contains rotated characteristic ellipsoids, at four evenly distributed heights from the toe to the surface, from $y = d_1$ to $y = d_1 + 0.75(d_2 - d_1)$ to provide a lucid explanation (refer to supplementary files to see ellipsoids throughout the surge front in all three cases of Froude numbers). These ellipsoids are plotted from $(x - ct)/d_2 = 0$ up to the surge front at nodes 0.025 m ($5\delta x_1$) apart from each other for clarity. The shape of each ellipsoid elucidates the dimension of turbulence at that location of the flow. The elongated

prolate ellipsoid indicates one-dimensionality, whereas the flattened oblate ellipsoid indicates two-dimensionality, and finally, a perfect sphere is for three-dimensional isotropic turbulence. These ellipsoids are rotated such that their major axes align with principal eigenvectors. At each height, the ellipsoids are shown from two planar views [Fig. 11(b) shows the three planar views of the setup]: the first row is the side view, and the second row is the top view. In Fig. 12, the first series of ellipsoids at the height of $y = d_1$ in all three Froude numbers illustrates the evolution of dimensionality and directionality of turbulence from the origin of the shear mixing layer, the toe, to further upstream. The initial few ellipsoids are predominantly elongated along the streamwise direction (x-axis in the Cartesian coordinates), implying one-dimensionality at the toe which was also shown in Sec. III E. The direction of the dominant eigenvalue indicated by the green vector is also aligned in the streamwise direction. Moving away from the toe, two radii of ellipsoids gain comparable magnitudes and the stretching reduces; nonetheless, the elongated prolate property persists throughout the series.

Focusing on the orientation of the ellipsoids starting from the toe, a transition of dominant eigenvector (green-colored vector) from the streamwise direction to an angle of $45°$, rotated in the clockwise direction about the z-axis, is evident as we move away from the toe. The positive shear stress $-\overline{u''v''}$ introduced in the wake of the surge due to the velocity gradient is the cause for this shift in orientation.
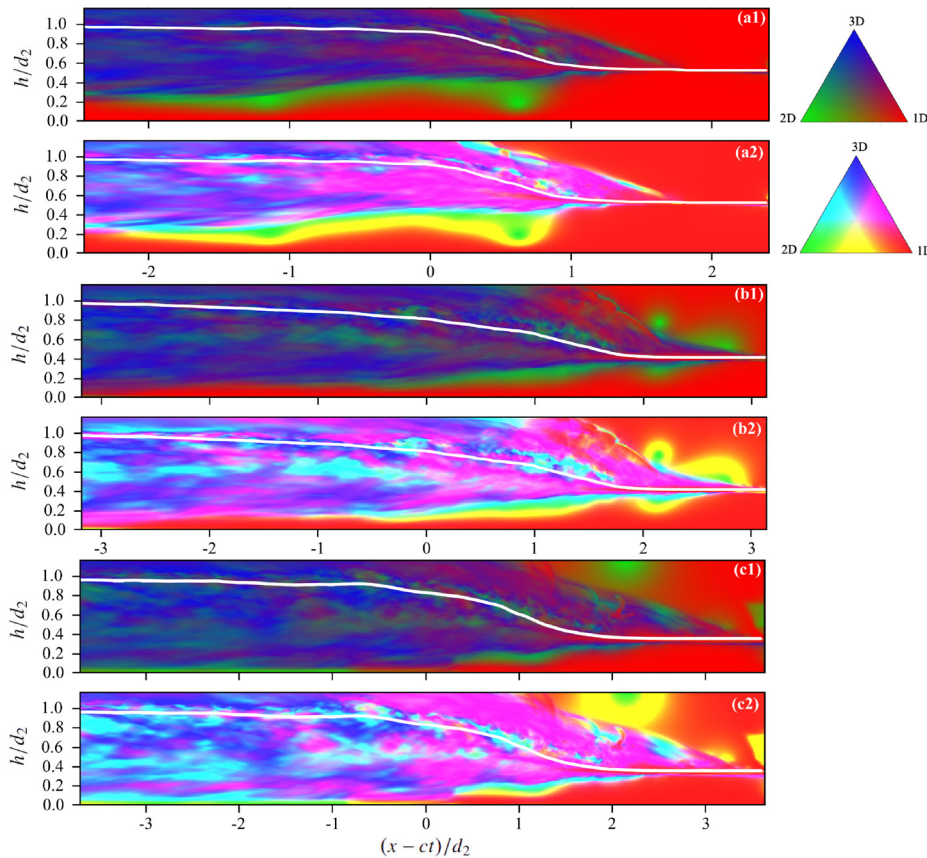
FIG. 10. (1) Conventional anisotropy color map and (2) modified anisotropy color map for (a) $Fr_s = 1.71$, (b) $Fr_s = 2.13$, and (c) $Fr_s = 2.49$.

However, the orientation of the other two vectors, i.e., the intermediate eigenvector (red-colored vector) and the smallest eigenvector (blue-colored vector), is mostly parallel to the z-axis and the y-axis of the Cartesian coordinates, respectively. This implies that the shear stresses $-\widetilde{u''w''}$ and $-\widetilde{v''w''}$ are negligible compared to the remaining stresses, thus not strong enough to alter the orientation of principal stresses. These stress magnitudes are also presented in Fig. 6 in the case of $Fr_s = 2.13$. These observations across the surge toe are consistent in all three Froude numbers presented in Fig. 12.

Moving on to the next series of ellipsoids at a height of $y = d_1 + 0.25(d_2 - d_1)$, the most pronounced differences from the previous observations are the first couple of ellipsoids between $(x - ct)/d_2 = 1.0$ and the surge front. In the previous series, the ellipsoids at the toe were predominantly elongated, whereas here, we see attenuation of that feature in all three cases of Froude numbers. In fact, some of the ellipsoids are closer to oblate in nature in the case of $Fr_s = 2.13$, which also agrees with the color maps shown previously in Sec. III E. Across this region, there are high perturbations and chaotic interactions between water and air. As a result, all the components of Reynolds stresses gain comparable magnitudes, and therefore, the ellipsoids are not as uni-directional as those across the toe.

In the previous discussion for $y = d_1$, the orientation increased from $0°$ (streamwise) to $45°$ about the z-axis as we move away from the toe; however, for $y = d_1 + 0.25(d_2 - d_1)$, we see that the orientation of ellipsoids decreases from a higher angle (close to $60°$–$70°$) to

$45°$, upstream. This is again associated with shear stress, $-\widetilde{u''v''}$. At this height, the shear stress begins with an imposing magnitude at the surge front and deteriorates with distance from the surge front, which is attributed to the aforementioned characteristics. On the contrary, at the toe height, the shear stress has not developed; consequently, the ellipsoids are not rotated off the streamwise direction close to the toe. The $Fr_s = 2.49$ case, from Fig. 12(c), is exceptional to this observation because the streamwise normal stress, $\widetilde{u''u''}$, is prevalent over the shear stress even at this height, i.e., $y = d_1 + 0.25(d_2 - d_1)$. Here, the angle does not exceed $45°$ throughout the series. Additionally, elongated ellipsoids are also seen at this height due to the same reason.

The third series at the height of $y = d_1 + 0.5(d_2 - d_1)$ shows quite similar characteristics to those discussed for the previous height. The final series, closest to the surface, are completely prolate in shape and show a uniform pattern in the orientation of eigenvectors. These ellipsoids are farthest from the toe of the surge where the shear mixing layer originates, both laterally and longitudinally. As a result, the stresses at this location are significantly smaller than in the remaining series which is why the ellipsoids are diminished in size. Nevertheless, the shear stress still persists at this height; thus, the ellipsoids are rotated about the z-axis.

Focusing on the zoomed view of ellipsoids at the toe region for all three Froude numbers in Fig. 12, there are two noticeable features regarding the shape and orientation of the characteristic shapes. First, the shapes are more outstretched along the streamwise direction in the
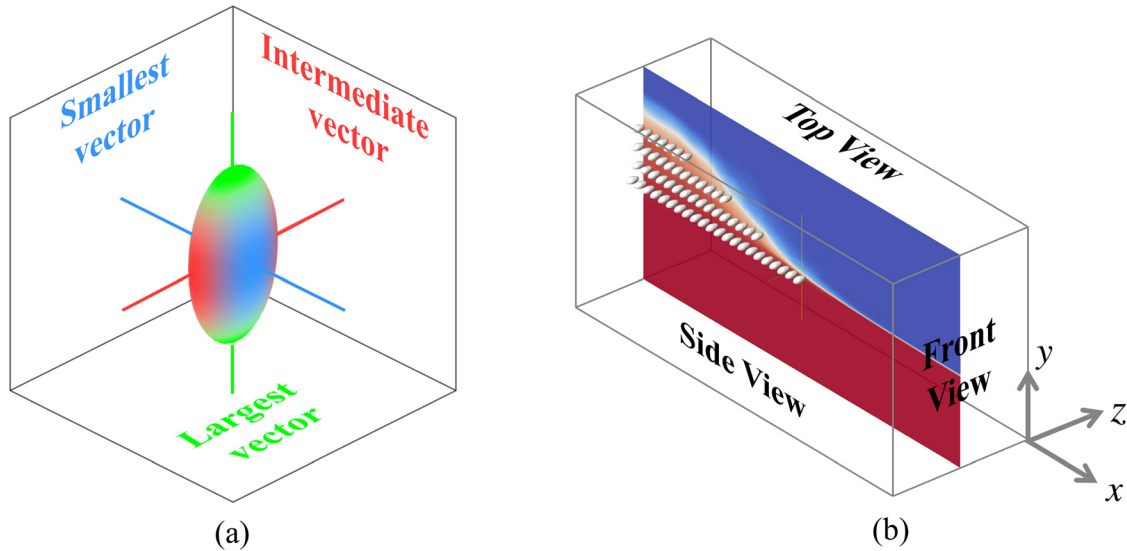
FIG. 11. (a) Colors assigned to eigenvectors and associated principal stresses and (b) the side view and top view of ellipsoids used in Fig. 12.

case of $Fr_s = 2.49$ compared to $Fr_s = 1.71$. This indicates that as the Froude number increases, the streamwise Reynolds stress is more dominant over other stresses leading to more anisotropic characteristics at the toe. Second, the ellipsoids are more closely aligned along the streamwise direction in the case of $Fr_s = 2.49$ compared to $Fr_s = 1.71$, which suggests that the shear stresses are trivial at the toe for higher Froude numbers. This inclination of ellipsoids at the toe toward the water surface, in the case $Fr_s = 1.71$, can also be seen in the supplementary material video of the Q-criterion showing the coherent structures of the mixing layer gravitating toward the surface.

Finally, an amusing feature from Fig. 12 is the orientation of the smallest (blue-colored vector) and intermediate (red-colored vector) principal stresses. These two vectors uncover two regimes of the surge front, namely, the recirculation (roller) region and the mixing layer (shear layer) region acknowledged in Sec. III A.

Having a close inspection of the side view of ellipsoids, i.e., the xy-plane, reveals that the color at the center of the ellipsoid shifts from blue, close to the surge front, to red away from the surge front upstream. Thus, it is obvious that the opposite happens in the top view of ellipsoids. The side view of ellipsoids initially shows blue color at its center implying that the shortest principal stress (blue-colored vector) is aligned along the z-axis (spanwise direction); hence, the intermediate principal stress (red-colored vector) is on the xy-plane. However, away from the surge front, the side view changes to red implying the converse. The second series, $y = d_1 + 0.25(d_2 - d_1)$, in Fig. 12 for all three cases exemplifies these observations.

The cluster of ellipsoids having its blue vector perpendicular to the xy-plane forms a unique regime along the free-surface of the surge front which is deemed to be the recirculating region of the surge. The transverse normal Reynolds stress, $\widetilde{v''v''}$, is predominant close to the surge front as shown in Fig. 6(b). Thus, the two foremost principal stresses lie on the xy-plane in the recirculating region, leading to the one parallel to the z-axis having the least magnitude. This is pertinent to high air entrainment in the roller region as a result of impingement

and deformation of the water surface caused by these turbulent structures. Based on the current analysis, this region does not commence immediately prior to the toe but is a few centimeters upstream from the toe in all three Froude numbers as seen in Fig. 12. This subtle gap between the turbulent roller and the surge toe is also mentioned by Chanson and Docherty,[49] where they noted a small time-lapse between the two in their data.

Similarly, the mixing layer region identified by clusters of red ellipsoids is formed below the recirculation region. The lower boundary of this layer is traced by the ellipsoids having stress magnitudes $0.005\ U_2^2$, below which the ellipsoids are unnoticeable and negligible. Identification of these two regions using ellipsoids is depicted in the supplementary contours having ellipsoids all across the surge front. This transition of colors is consistent in all three heights of ellipsoids except the first series at the height of $y = d_1$ in all Froude numbers as it lies entirely in the mixing layer region. The recirculation region has not developed at this height; therefore, $\widetilde{v''v''}$ is negligible which is also seen in Fig. 6(b). Thus, the red color in the side view and the blue color in the top view remain unchanged throughout the series of ellipsoids.

IV. LARGE EDDY SIMULATIONS: CONVERGENCE AND KOLMOGOROV SCALE

Current study implements the k-equation LES model, where smaller than grid scale perturbations are modeled and larger resolved. The combined modeling and discretization approach implemented in this study is designed to: (i) meet the recommendation related to scale and TKE resolution[50,51] and (ii) attain the convergence required for verification, which is the pragmatic approach for estimating errors and uncertainties in such simulations.[52] This section expands on these criteria and discusses the present results within the scope of these principles.

A. Kolmogorov scale and LES resolution

The resolution of the simulation plays a key role in the performance of LES. As demonstrated in Appendix A, the current
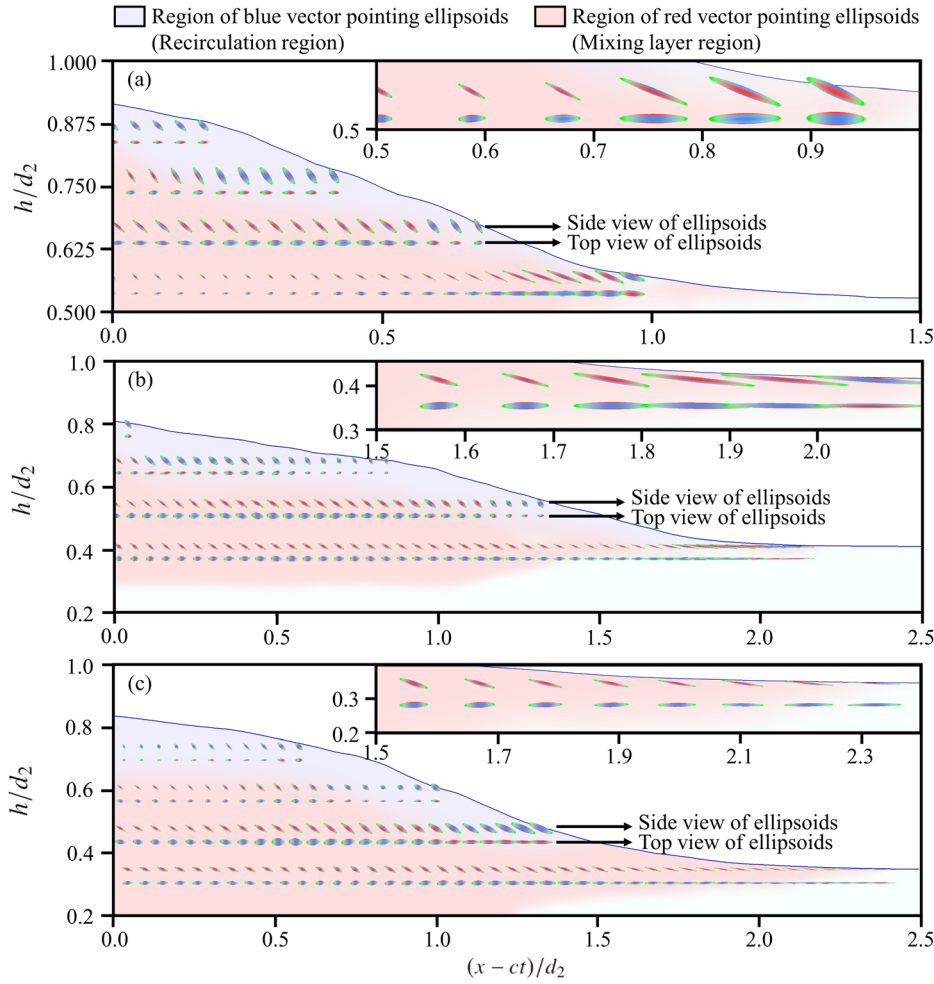
FIG. 12. Characteristic ellipsoids for (a) $Fr_s = 1.71$, (b) $Fr_s = 2.13$, and (c) $Fr_s = 2.49$ at nodes 0.025 m ($5\delta x_1$) apart. Inset in each FIG shows the zoomed view at the toe region of the surge constituting ellipsoids at nodes 0.05 m ($10\delta x_1$) apart for better visualization. At each height, the ellipsoids are shown from two planar views: the first row is the side view, and the second row is the top view.

simulation resolves the smallest Hinze scale in the domain located near the toe. To assess LES performance, first, the Kolmogorov scale is obtained using turbulent dissipation. The expression of the Kolmogorov length scale is given as

$$\eta \equiv \left(\nu^3 / \varepsilon \right)^{1/4}, \tag{24}$$

where ν is the kinematic viscosity. Furthermore, the first Kolmogorov hypothesis introduces another length scale, l_{EI}, which is the demarcation of the production regime. Scales between η and l_{EI} fall into the universal equilibrium regime. The universal regime is further divided into the inertial subrange ($l_{DI} < l < l_{EI}$), where the inertial effects are dominant, and the dissipation range ($\eta < l < l_{DI}$), where viscous effects are dominant, thus dissipation takes place. This distinction is made by a length scale, defined by Pope[50] as $l_{DI} = 60\eta$. The Kolmogorov length scale at the toe of the surge having the maximum value of dissipation is estimated to be $2.627 \times 10^{-4} d_2$ (dimensionally 1.348×10^{-4} m). Thus, the corresponding $l_{DI} = 60\eta$ is $1.576 \times 10^{-2} d_2$ (dimensionally 8.088×10^{-3} m). According to Pope,[50] the ideal filter size of LES must be smaller than l_{EI}. This condition is clearly satisfied as the filter size is even smaller than l_{DI}. Thus, the grid resolution is adequate in terms of bubble as well as eddy sizes. The quality of LES is further reinforced by

demonstrating that the majority of the kinetic energy is resolved in the current simulation (Appendix C).

B. Convergence criteria

To further corroborate the results, we conducted a grid-refinement study for a surge Froude number of $Fr_s = 2.13$. This analysis is conducted for the following Favre-averaged stress term, $\tau_{xy-\text{avg}}$, over an area of interest that is confined to $0 < (x - ct)/d_2 < 2$:

$$\tau_{xy-\text{avg}} = \frac{1}{1.2d_2} \sum_{(x-ct)=0}^{2d_2} \sum_{h=0}^{0.6} -\bar{\rho}\widetilde{u''v''}\delta^2. \tag{25}$$

The order of convergence, P_k, is accordingly calculated based on the method used by Karimpour and Chu[4] and Karimpour et al.[53] as

$$P_k = \frac{1}{\ln r} \ln \left(\frac{\tau_{xy-\text{avg}(k)} - \tau_{xy-\text{avg}(k-1)}}{\tau_{xy-\text{avg}(k+1)} - \tau_{xy-\text{avg}(k)}} \right), \tag{26}$$

where $k - 1$, k, and $k + 1$ denote the simulation results obtained from the sequential refinement of the grid. The ratio of refinement, r, is $r = 1.25$, in the present study, for cases 2–1, 2–2, and 2–3. The

TABLE II. The mesh refinement study for the surge Froude number of $Fr_s = 2.13$ (cases 2-1, 2-2, and 3-3) conducted on spatially averaged resolved turbulent stress based on Eq. (25), τ_{xy-avg}, with a refinement ratio of $r = 1.25$.

Case ID	$N = 1.0/\delta x_2$	$\tau_{xy-avg}/\rho_w U_2^2$	Order (P_k)	$FE(\%)$
2–1	320	0.007 832 1	$\cdots$	5.96
2–2	400	0.007 676 4	1.954	3.85
2–3	500	0.007 575 8	$\cdots$	2.49

estimated "exact" value is extrapolated, and the Fractional Error (FE) for each of the three simulations is defined accordingly. Table II reports the properties as well as the convergence parameters for each of the three cases. The results presented in this paper are mainly based on the grid resolution of $N = 1.0/\delta x_2 = 400$, near the surge toe. This grid refinement study demonstrates an expected FE of 3.85% for the results. Furthermore, the fractional computation error for this averaged resolved turbulent stress term is as expected because it is lower than the highest order of TVD scheme used for the phase and spatial interpolation scheme of the momentum flux terms.

V. SUMMARY AND CONCLUSION

The scope of this paper is to highlight the existence of a wide array of turbulent anisotropic features across three-dimensional two-phase breaking surge waves. This numerical study focuses on weak breaking surge waves, where the surge Froude number is higher than 1.7, which is the upper range for undular waves while limited to 2.5. This distinction was made to mainly focus on the turbulent flow features across the mixing region and the breaking recirculating front while minimizing the impact of the boundary layer. Here, we generated transient surge waves using the initial setup of a dam-break wave and resolved tempo-spatial characteristics of the flow using combined LES and VOF. The mesh resolution is defined to capture a wide spectrum of flow scales down to the Hinze scale for bubbles while satisfying the LES quality.[50,51] The results have demonstrated a good agreement with existing experiments, illustrating the validity of the results. Some of the key observations and conclusions in this work are:

- Resolved TKE production across the surge front was prevalent in the mixing layer region. Furthermore, the production term contributing to the normal streamwise turbulent stress was dominant, and its peak occurred near the toe. By decomposing the production terms, we have demonstrated that the velocity gradient is the principal driver of high production of TKE behind the toe. Moreover, we have observed small but negative resolved TKE near the air–water interface. A similar observation was made by Wei et al.[10] near the free surface for undular hydraulic jumps. These features were persistent in all Froude numbers.

- Overall distinguishable features and peculiar ones at the interface and surge toe were observed in turbulent stresses and total production when comparing Favre and constant density Reynolds averaging frameworks, particularly near the interface and the toe regions. This was attributed to the role of density fluctuations and the significance of turbulent mass flux terms in these regions. Although challenging, these results demonstrate the need for experimental techniques enabling the simultaneous measurement of the phase and velocity.[54–56] Furthermore, this comparative

analysis highlights the importance of incorporating terms related to density fluctuations in the Reynolds averaging framework for studies on breaking bores, surge waves, and hydraulic jumps.

- The color maps in the Barycentric triangle demonstrated evidence of a one-dimensional state in the vicinity of the toe for all three Froude numbers. This is in principle at the core, where the mixing layer is originated and where the maximum resolved TKE production was reported. Near the air–water interface, the prolate dominant state in the wake of the surge gradually shifted to a mixture of oblate and prolate near the heel. Behind the surge front, mainly three-dimensional colors were observed, indicating a gradual return to isotropy. This area of nearly isotropic behavior was observed closer to the surge front for higher Froude numbers.

- We have further assessed turbulent stress tensors by establishing the characteristic shape maps behind the surge wave for all three Froude numbers. This was achieved by pointwise eigendecomposition of the Reynolds stress tensor, computing its principal stresses and the associated eigenvectors. These characteristic ellipsoids reveal features, such as the degree and direction of anisotropy, which cannot be delineated using anisotropy invariant maps. Additionally, these maps provide insight into the 3D orientation of principal stresses beyond its shape. In reference to the Cartesian coordinate, Fig. 12 showed that the prolate ellipsoid near the toe is stretched mainly in the x-direction. In the mixing layer, at the toe level, this state rotated about the z-axis from the streamwise direction to 45°, which is caused by the dominance of $-\widetilde{u''v''}$ shear stress over $-\widetilde{u''w''}$ and $-\widetilde{v''w''}$, also seen in Fig. 6. This angle further exceeded 45° within the recirculation region, near the interface at shallower depths.

- In the recirculating region, the cluster ellipsoids in the side view showed a peculiar but consistent trait, where the smallest principal stress was aligned with the z-axis. As a result, the largest and intermediate principal stresses were on the xy-plane transcending the surface tension, leading to higher air entrainment. Below this region, in the mixing zone, the orientation was the inverse, where the intermediate principal stress was aligned in the z-direction. This indicates very distinct mixing features, one originating from a streamwise shear-induced mixing layer, and another caused by phase discontinuity leading to air entrainment at the interface. These features are detected in all three Froude numbers included in the study.

Using highly resolved LES simulations, we have provided a comprehensive characterization of turbulence and assessment of anisotropic features across the mixing layer and the recirculating region in breaking weak surge waves, including its connection with the production terms. This study also illustrates the need for LES, and if feasible DNS, for this flow and cautions against the use of turbulent models that are inherently based on the assumption that turbulence is locally isotropic.[50] In terms of the turbulent kinetic energy (k) budget, the study focuses on the decomposition of the production term to formulate the source of k and explain the linkage between the source and anisotropy. Further analysis is required to investigate other terms in the transport equation for the resolved turbulent kinetic energy, to enhance our understanding of energy budget in this transient two-phase flow. Furthermore, with its current setup, this study has the limitation of extending to higher Froude numbers beyond weak surge

14 November 2024 05:38:19

waves. This is mainly due to the resolution near the bed, where LES does not adequately address the development of the boundary layer and its interaction with the mixing region.

ACKNOWLEDGMENTS

AUTHOR DECLARATIONS
Conflict of Interest

The authors have no conflicts to disclose.

Author Contributions

Akash Venkateshwaran: Data curation (equal); Formal analysis (equal); Investigation (equal); Validation (equal); Visualization (equal); Writing – original draft (equal). **Zhuoran Li:** Conceptualization (supporting); Data curation (equal); Methodology (equal); Resources (equal); Software (equal); Visualization (equal); Writing – original draft (equal). **Shooka Karimpour:** Conceptualization (lead); Funding acquisition (lead); Resources (lead); Software (lead); Supervision (lead); Writing – original draft (supporting).

DATA AVAILABILITY

The data that support the findings of this study are available within the article.

APPENDIX A: HINZE SCALE

Air bubbles are entrained into the water at the surge front and have different scales. Once entrained, these bubbles cannot be sustained by the surface tension, hence rapidly break into smaller bubbles due to the turbulent forces. This break-down process continues until the surface tension force gains comparable strength, to a point where the balance between the turbulent kinetic energy of the flow and interfacial energy is reached. The scale of the bubble at this point is defined as the Hinze scale, which implies the smallest size to which turbulent forces can fragment bubbles. The Hinze scale is defined as

$$D_H = C \left(\frac{\sigma}{\rho_w} \right)^{3/5} \varepsilon^{-(2/5)}, \tag{A1}$$

where $C = 0.725$ is a constant of proportionality from Hinze,[57] calculated using the experimental data of Clay.[58] Clay[58] determined the bubble-size distribution and D_{95} such that 95% of the droplets have diameters below D_{95}. Hinze used this scale as the maximum bubble size to decide the aforementioned constant. In this equation, σ is the surface tension coefficient between air and water, ρ_w is the density of water, and ε is the dissipation of the turbulent kinetic energy formulated from term (3) in Eq. (13).

Figure 13 shows the Hinze scale normalized by d_2 and the ratio of the grid size, δ, over the Hinze scale. The Hinze scale from Eq. (A1) is closely related to the dissipation of the turbulent kinetic energy. The dissipation field emanates from the toe of the surge
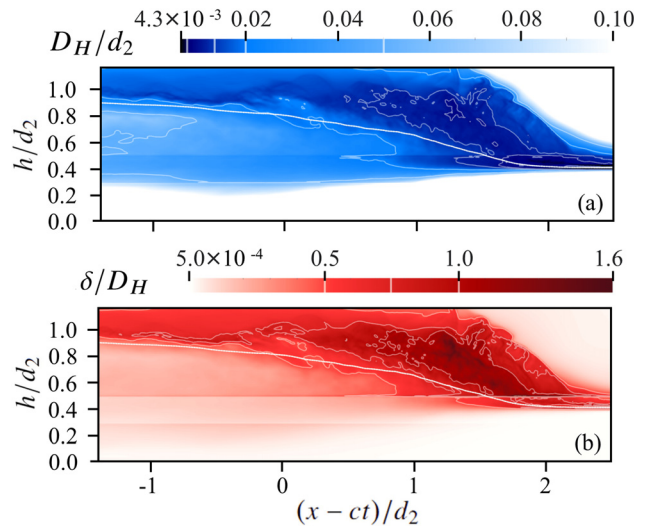

FIG. 13. (a) Hinze scale normalized by d_2 with contours lines at 0.0075, 0.01, 0.02, and 0.05 and (b) the ratio of the grid size over the Hinze scale with contours lines at 0.50, 0.75, and 1.00 for $Fr_s = 2.13$.

bore and progressively degrades upstream. Its peak is observed at the origin of the shear mixing layer which is the toe of the surge bore. Thus, as expected, the minimum Hinze scale of the two-phase flow having a magnitude of $0.0043d_2$ (dimensionally 2.2 mm) is in the corresponding location. The contour lines at $0.0075d_2$, $0.01d_2$, $0.02d_2$, and $0.05d_2$ are overlaid for better visualization of the different regimes of the Hinze scale. These contour lines divide the surge front region into four parts: the toe having scales less than $0.0075d_2$ demarcated by the $0.0075d_2$ contour line, followed by bubble sizes less than $0.01d_2$ and subsequently $0.02d_2$, while the $0.05d_2$ contour line outlines the border of the shear mixing layer. The ratio of the mesh size, δ, to the Hinze scale, D_H, in Fig. 13 incorporates mesh size variability as the computational domain. The ratio in the region below the surge front is always less than one, spanning between 0.5 and 0.75 close to the toe and the interface, indicating that the grid size is consistently smaller than the Hinze scale. In contrast, the ratio just outside the Area of Refinement 2 (AR2), in the air region, is greater than one having a maximum value of 1.6. Nonetheless, the contour plots demonstrate that the resolution of LES filter is less than the Hinze scale below the air–water interface and above this interface is less or at least commensurate with the smallest bubble size. In other words, in the current simulation for the flow below the air–water interface, scales above the Hinze scale are resolved. However, to further resolve the interface features to scales below the Hinze scale, inclusion of surface tension in the governing equations is necessary.[59]

APPENDIX B: VALIDATION

In this section, we endeavor to compare our analysis with the experimental results presented by Leng and Chanson[60] and Murzyn et al.[61] and provide a reliable validation test. We would like to acknowledge that the exact Froude numbers presented in this paper

are not experimentally available. In our analysis for void fraction, we relied on the Froude number nearest to our setup. Furthermore, analyses by Murzyn *et al.*[61] were conducted for stationary hydraulic jumps, but we nevertheless relied on their semi-empirical equations for volume fraction, simply due to analogy of moving surge waves with hydraulic jumps, as outlined earlier in the paper. Two additional validation tests are conducted, i.e., the maximum instantaneous free-surface fluctuations, and the time lag between the peak Reynolds stress and free-surface fluctuation as a function of the Froude number. In these validations, we relied on correlation functions of Froude numbers provided in Leng and Chanson.[60]

1. Air distribution profile

In their study, Murzyn *et al.*[61] investigated the distribution of air in the two-phase flow across hydraulic jumps of Froude numbers ranging from 2 to 8.5. Their measurements were carried out using dual optical sensors. Following analysis, Murzyn *et al.*[61] identified two regimes: the lower region (shear layer) and the upper region (roller region). Near the toe, the air entrainment is governed by the shear layer (also see Chanson[62]) where the mean velocity dominates over the bubble rise velocity, while in the upper region, the air distribution is governed by interfacial interactions and recirculating mechanism.

Since, in the shear region, the air distribution is governed by advection–diffusion, Chanson[62] and Murzyn *et al.*[61] proposed that the void fraction, the air volume fraction in the present study, in depth can be expressed by a Gaussian profile

$$\alpha_a = \alpha_{a-\max} \exp\left(-\frac{1}{4}\frac{U}{D}\frac{(y - y_{\max})^2}{x_t - x}\right), \tag{B1}$$

where x_t is the position of the toe, and $(x_t - x)$ represents the streamwise distance from the toe. $\alpha_{a-\max}$ is the maximum air volume fraction reported at $y_{\max}$ at selective streamwise locations, and D is the diffusion coefficient. The expression for the void fraction in the upper region is given by Brattberg *et al.*[63] as

$$\alpha_a = \frac{1}{2}\left[1 + \mathrm{erf}\left(\frac{(y - y_{\alpha 50})}{2\sqrt{D(x_t - x)/U}}\right)\right], \tag{B2}$$

where $\alpha_a = 0.5$ at the vertical position of $y_{\alpha 50}$. Murzyn *et al.*[61] have reported the experimental values for D/Ud_1, $y_{\max}/d_1$, and $y_{\alpha 50}/d_1$ for Froude numbers of 2.0, among other Froude numbers. Using these parameters for the surge Froude number of $Fr_s = 2.13$, ensemble-averaged air volume fraction profiles are plotted at selective streamwise locations of $(x_t - x)/d_1 = 0.85, 1.70, 2.54,$ and 4.27.

A plot of ensemble-averaged air volume fraction, α_a, is provided in the 2–2 case with $Fr_s = 2.13$ and compared with Eqs. (B1) and (B2). Figure 14(a) shows that the profiles obtained from the present simulations for the shear region nearly collapse on the empirical profile and match well with the Gaussian profile shown in Eq. (B1).

For the upper region, all three profiles are in good agreement with Eq. (B2). The volume fraction distribution breaks away from Eq. (B2) when $\alpha_a < 0.5$ [bottom of the upper region profile in Fig. 14(b)], indicating the transition to the lower region governed by the previous equation as expected. This deviation is larger in profiles at longer streamwise distances from the toe, with greater distances from the shear layer origin.
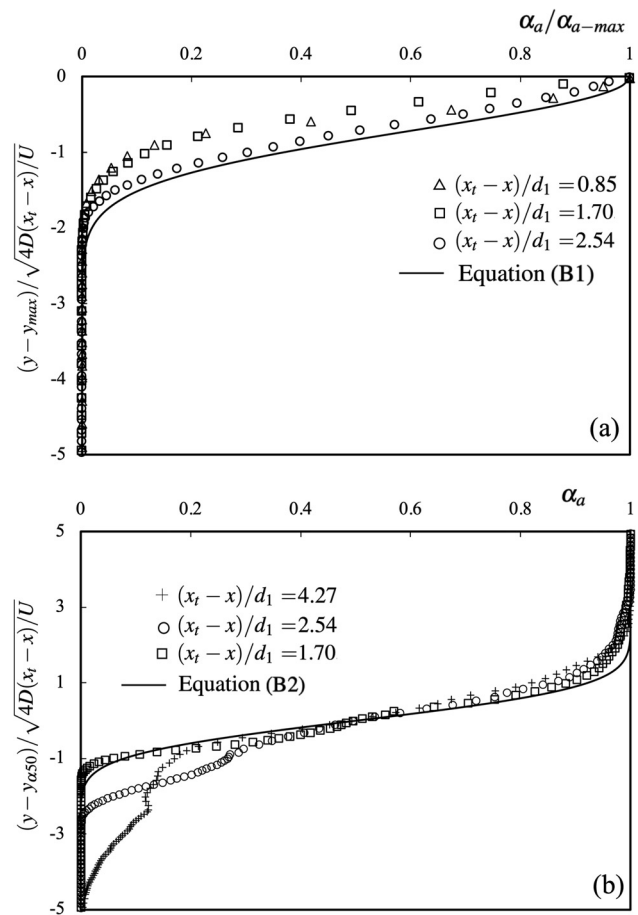

FIG. 14. Air volume fraction profile in the (a) lower region (shear layer) and (b) upper region (roller region) compared with Eqs. (B1) and (B2) proposed by Murzyn *et al.*[61] and Brattberg *et al.*,[63] respectively.

2. Maximum free-surface perturbation and lag time in Reynolds stresses

Leng and Chanson[60] constitute 25 ensemble-averaged data yielding the fluctuation in free-surface elevation and turbulent Reynolds stresses. They characterized the fluctuation in free-surface elevation as the difference in the third, d_{75}, and first quartile, d_{25}, of the instantaneous surface height data. The maximum fluctuation in surface height, $(d_{75} - d_{25})_{\max}$, as a function of the Froude number was empirically interpolated as

$$\frac{(d_{75} - d_{25})_{\max}}{d_1} = 0.331 \times (Fr_s - 1)^{0.63} \quad \text{for } 1.38 < Fr_s < 2.2. \tag{B3}$$

Additionally, they compared the time lag (ΔT) between the arrival of the bore and peak Reynolds stresses and the time lag (Δt) between the arrival of the bore and peak free-surface fluctuations. The correlation function of the ratio of these two time lags with respect to the surge Froude number was defined as
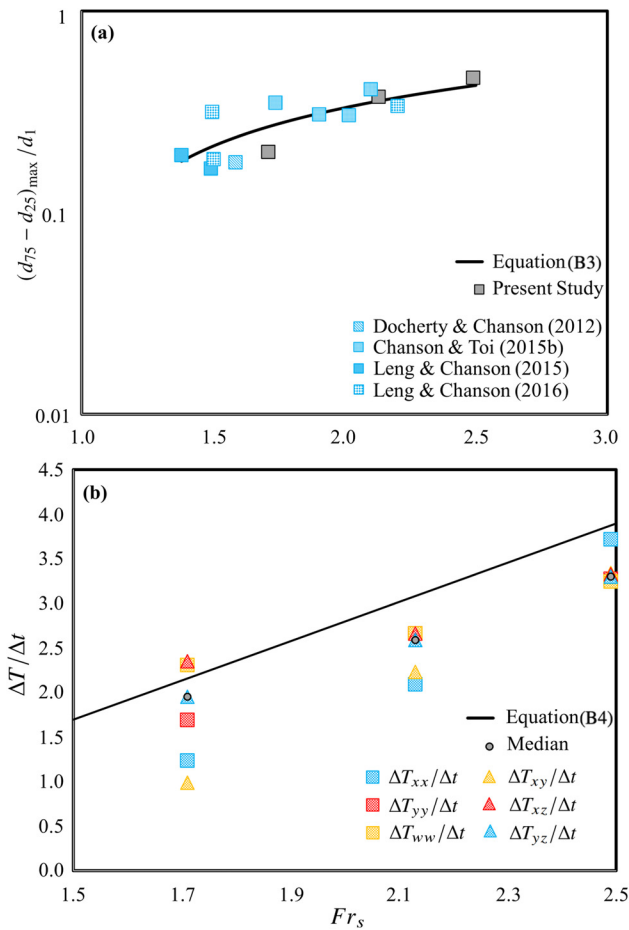
FIG. 15. Validation tests for three Froude numbers: (a) maximum free-surface fluctuations normalized by d_1 compared with Eq. (B3) and experiments and (b) the ratio of time lags in six Reynolds stresses and their median compared with Eq. (B4).

$$\frac{\Delta T}{\Delta t} = 2.2 \times (Fr_s - 0.73) \quad \text{for } 1.2 < Fr_s < 2.2. \tag{B4}$$

These two functions are compared with the three Froude numbers presented in this paper in Fig. 15. Although in case no. 3 the Froude number of $Fr_s = 2.49$ is outside the limits mentioned in Eqs. (B3) and (B4), it is not prohibitively off range enough to deviate from the correlation trend. The free-surface fluctuation follows the same trend as Eq. (B3), where the ratio increases as the Froude number increases. Similarly, the time lag ratio is also consistent with the experimentally derived Eq. (B4). Overall, these validation tests demonstrate a good agreement with the experiment, illustrating the validity of the results presented in this paper.

APPENDIX C: LES RESOLUTION

A widely used method to estimate the quality of LES results was introduced by Pope,[50] where the majority of the turbulent kinetic energy should be resolved in LES, while only a fraction are left to LES modeling and residual stresses. Matheou and Chung[51] and Pope[50] proposed that the resolved TKE, k, should be more than 80% and 90% of the total TKE, respectively, to enable a well-resolved simulation. Here, the total TKE is estimated using k and k_R.

As shown in Fig. 16, our simulations have consistently achieved more than 80% resolution, even near the critical regions, such as the toe and the air–water interface. Highlights of white shade can be seen above and along the air–water interface, indicating a resolution close to 80%. Splashing and spattering of water are common at the free-surface, which lead to droplets of water that are unresolved due to their small sizes. Since Favre averaging, implemented in this study, emphasizes the water property over air as discussed in Sec. III D, these modeled stresses accumulate over averaging and become protrusive. As a result, white irregular contours are prominent at the top of the black line.
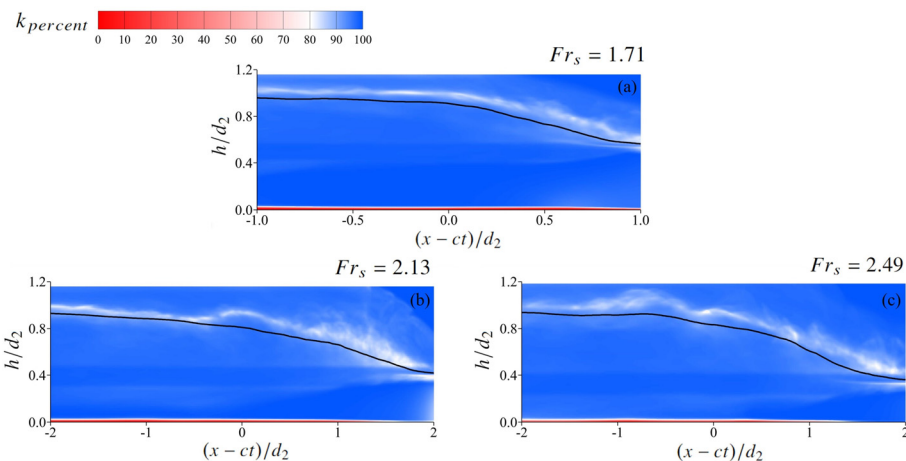

FIG. 16. Ratio of the resolved to total TKE in current simulations for surge Froude numbers of (a) $Fr_s = 1.71$, (b) $Fr_s = 2.13$, and (c) $Fr_s = 2.49$.

REFERENCES

[1] N. Khezri and H. Chanson, "Inception of bed load motion beneath a bore," Geomorphology **153–154**, 39–47 (2012).

[2] S. F. Greb and A. W. Archer, "Soft-sediment deformation produced by tides in a meizoseismic area, Turnagain Arm, Alaska," Geology **35**, 435–438 (2007).

[3] P. Xie and V. H. Chu, "The forces of tsunami waves on a vertical wall and on a structure of finite width," Coastal Eng. **149**, 65–80 (2019).

[4] S. Karimpour and V. H. Chu, "High-order interpolation schemes for shear instability simulations," Int. J. Numer. Methods Heat Fluid Flow **25**, 1340–1360 (2015).

[5] H. Chanson, D. Reungoat, B. Simon, and P. Lubin, "High-frequency turbulence and suspended sediment concentration measurements in the Garonne River tidal bore," Estuarine, Coastal Shelf Sci. **95**, 298–306 (2011).

[6] C. Lin, S.-C. Hsieh, I.-J. Lin, K.-A. Chang, and R. V. Raikar, "Flow property and self-similarity in steady hydraulic jumps," Exp. Fluids **53**, 1591–1616 (2012).

[7] M. Mortazavi, V. Le Chenadec, P. Moin, and A. Mani, "Direct numerical simulation of a turbulent hydraulic jump: Turbulence statistics and air entrainment," J. Fluid Mech. **797**, 60–94 (2016).

[8] H. Chanson and Y. H. Toi, "Physical modelling of breaking tidal bores: Comparison with prototype data," J. Hydraul. Res. **53**, 264–273 (2015).

[9] X. Leng, B. Simon, N. Khezri, P. Lubin, and H. Chanson, "CFD modeling of tidal bores: Development and validation challenges," Coastal Eng. J. **60**, 423–436 (2018).

[10] M. Wei, Y.-M. Chiew, and A. Emadzadeh, "Flow patterns and turbulent kinetic energy budget of undular jumps in a narrow flume," J. Hydraul. Eng. **146**, 04020060 (2020).

[11] J. Lennon and D. Hill, "Particle image velocity measurements of undular and hydraulic jumps," J. Hydraul. Eng. **132**, 1283–1294 (2006).

[12] E. Mignot and R. Cienfuegos, "Energy dissipation and turbulent production in weak hydraulic jumps," J. Hydraul. Eng. **136**, 116–121 (2010).

[13] D. Wüthrich, R. Shi, and H. Chanson, "Strong free-surface turbulence in breaking bores: A physical study on the free-surface dynamics and air–water interfacial features," J. Fluid Mech. **924**, A20 (2021).

[14] X. Leng and H. Chanson, "Integral turbulent scales in unsteady rapidly varied open channel flows," Exp. Therm. Fluid Sci. **81**, 382–395 (2017).

[15] H. Wang and F. Murzyn, "Experimental assessment of characteristic turbulent scales in two-phase flow of hydraulic jump: From bottom to free surface," Environ. Fluid Mech. **17**(1), 7–25 (2017).

[16] Y. Chachereau and H. Chanson, "Free-surface fluctuations and turbulence in hydraulic jumps," Exp. Therm. Fluid Sci. **35**, 896–909 (2011).

[17] Z. Li, A. Venkateshwaran, and S. Karimpour, "Turbulent characteristics and air entrainment patterns in breaking surge waves," Fluids **6**, 422 (2021).

[18] O. Kimmoun and H. Branger, "A particle image velocimetry investigation on laboratory surf-zone breaking waves over a sloping beach," J. Fluid Mech. **588**, 353–397 (2007).

[19] Y. Watanabe, H. Saeki, and R. J. Hosking, "Three-dimensional vortex structures under breaking waves," J. Fluid Mech. **545**, 291–328 (2005).

[20] P. Lubin and S. Glockner, "Numerical simulations of three-dimensional plunging breaking waves: Generation and evolution of aerated vortex filaments," J. Fluid Mech. **767**, 364–393 (2015).

[21] M. Derakhti and J. T. Kirby, "Bubble entrainment and liquid–bubble interaction under unsteady breaking waves," J. Fluid Mech. **761**, 464–506 (2014).

[22] M. Emory and G. Iaccarino, "Visualizing turbulence anisotropy in the spatial domain with componentality contours," in *Center for Turbulence Research Annual Research Briefs* (Stanford University, 2014), pp. 123–138.

[23] S. Banerjee, R. Krahl, F. Durst, and C. Zenger, "Presentation of anisotropy properties of turbulence, invariants versus eigenvalue approaches," J. Turbul. **8**, N32 (2007).

[24] A. Yoshizawa and K. Horiuti, "A statistically-derived subgrid-scale kinetic energy model for the large-eddy simulation of turbulent flows," J. Phys. Soc. Jpn. **54**, 2834–2839 (1985).

[25] S. Almeland, "Implementation of an air-entrainment model in interFoam," Proceedings of CFD with OpenSource Software, edited by H. Nilsson (2018).

[26] P. Cifani, W. Michalek, G. Priems, J. G. Kuerten, C. van der Geld, and B. J. Geurts, "A comparison between the surface compression method and an interface reconstruction method for the VOF approach," Comput. Fluids **136**, 421–435 (2016).

[27] C. J. Greenshields "Openfoam user guide," version 3(1), 47 (OpenFOAM Foundation Ltd., 2015).

[28] M. Saeedipour, S. Vincent, and S. Pirker, "Large eddy simulation of turbulent interfacial flows using approximate deconvolution model," Int. J. Multiphase Flow **112**, 286–299 (2019).

[29] S. Vincent, J. Larocque, D. Lacanette, A. Toutant, P. Lubin, and P. Sagaut, "Numerical simulation of phase separation and *a priori* two-phase LES filtering," Comput. Fluids **37**, 898–906 (2008).

[30] M. Herrmann, "A sub-grid surface dynamics model for sub-filter surface tension induced interface dynamics," Comput. Fluids **87**, 92–101 (2013).

[31] M. Klein, S. Ketterl, and J. Hasslberger, "Large eddy simulation of multiphase flows using the volume of fluid method: Part 1—Governing equations and *a priori* analysis," Exp. Comput. Multiphase Flow **1**, 130–144 (2019).

[32] T. Cai, *Tsunamis: Economic Impact, Disaster Management and Future Challenges* (Nova Science Publishers, 2013).

[33] A. Iafrati, "Numerical study of the effects of the breaking intensity on wave breaking flows," J. Fluid Mech. **622**, 371–411 (2009).

[34] G. Chen, C. Kharif, S. Zaleski, and J. Li, "Two-dimensional Navier–Stokes simulation of breaking waves," Phys. Fluids **11**, 121–133 (1999).

[35] H. Chanson, *Hydraulics of Open Channel Flow* (Elsevier, 2004).

[36] G. R. Tabor and M. Baba-Ahmadi, "Inlet conditions for large eddy simulation: A review," Comput. Fluids **39**, 553–567 (2010).

[37] W. Munters, C. Meneveau, and J. Meyers, "Shifted periodic boundary conditions for simulations of wall-bounded turbulent flows," Phys. Fluids **28**, 025112 (2016).

[38] X. Leng and H. Chanson, "Air-water interaction and characteristics in breaking bores," Int. J. Multiphase Flow **120**, 103101 (2019).

[39] Y. Ling, D. Fuster, G. Tryggvason, and S. Zaleski, "A two-phase mixing layer between parallel gas and liquid streams: Multiphase turbulence statistics and influence of interfacial instability," J. Fluid Mech. **859**, 268–307 (2019).

[40] M. J. Dwyer, E. G. Patton, and R. H. Shaw, "Turbulent kinetic energy budgets from a large-eddy simulation of airflow above and within a forest canopy," Boundary-Layer Meteorol. **84**, 23–43 (1997).

[41] B. Aupoix, G. Blaisdell, W. C. Reynolds, and O. Zeman, "Modeling the turbulent kinetic energy equation for compressible, homogeneous turbulence," in *Proceedings of the 1990 Summer Program* (Stanford University, 1990), pp. 63–74.

[42] S. K. Misra, J. T. Kirby, M. Brocchini, F. Veron, M. Thomas, and C. Kambhamettu, "The mean and turbulent flow structure of a weak hydraulic jump," Phys. Fluids **20**, 035106 (2008).

[43] A. Favre, *Problems of Hydrodynamics and Continuum Mechanics* (Society of Industrial and Applied Mathematics, 1969).

[44] K. Hendrickson and D. K.-P. Yue, "Wake behind a three-dimensional dry transom stern. Part 2. Analysis and modelling of incompressible highly variable density turbulence," J. Fluid Mech. **875**, 884–913 (2019).

[45] P. Chassaing, R. Antonia, F. Anselmet, L. Joly, and S. Sarkar, *Variable Density Fluid Turbulence* (Springer Science & Business Media, 2002), Vol. 69.

[46] J. L. Lumley and G. R. Newman, "The return to isotropy of homogeneous turbulence," J. Fluid Mech. **82**, 161–178 (1977).

[47] K. Nadaoka, M. Hino, and Y. Koyano, "Structure of the turbulent flow field under breaking waves in the surf zone," J. Fluid Mech. **204**, 359–387 (1989).

[48] C. Koch and H. Chanson, "Turbulence measurements in positive surges and bores," J. Hydraul. Res. **47**, 29–40 (2009).

[49] H. Chanson and N. J. Docherty, "Turbulent velocity measurements in open channel bores," Eur. J. Mech., B/Fluids **32**, 52–58 (2012).

[50] S. B. Pope, *Turbulent Flows* (Cambridge University Press, 2000).

[51] G. Matheou and D. Chung, "Large-eddy simulation of stratified turbulence. Part II: Application of the stretched-vortex model to the atmospheric boundary layer," J. Atmos. Sci. **71**, 4439–4460 (2014).

[52] F. Stern, R. V. Wilson, H. W. Coleman, and E. G. Paterson, "Comprehensive approach to verification and validation of CFD simulations—Part 1: Methodology and procedures," J. Fluids Eng. **123**, 793–802 (2001).

[53] S. Karimpour, T. Wang, and V. H. Chu, "The exchanges between the mainstream in an open channel and a recirculating flow on its side at large Froude numbers," J. Fluid Mech. **920**, A8 (2021).

[54] P. Ramaprabhu and M. J. Andrews, "Simultaneous measurements of velocity and density in buoyancy-driven mixing," Exp. Fluids **34**(1), 98–106 (2003).

[55]H. Lin, Y. Shi-He, T. Li-Feng, C. Zhi, and Z. Yang-Zhu, "Simultaneous density and velocity measurements in a supersonic turbulent boundary layer," Chin. Phys. B **22**, 024704 (2013).

[56]M. Raffel, "Background-oriented Schlieren (BOS) techniques," Exp. Fluids **56**, 1–17 (2015).

[57]J. O. Hinze, "Fundamentals of the hydrodynamic mechanism of splitting in dispersion processes," AIChE J. **1**, 289–295 (1955).

[58]P. Clay, "The mechanism of emulsion formation in turbulent flow: Theoretical part and dissuasion," Proc. R. Acad. Sci. **43**, 852–979 (1940).

[59]A. Rivière, W. Mostert, S. Perrard, and L. Deike, "Sub-Hinze scale bubble production in turbulent bubble break-up," J. Fluid Mech. **917**, A40 (2021).

[60]X. Leng and H. Chanson, "Coupling between free-surface fluctuations, velocity fluctuations and turbulent Reynolds stresses during the upstream propagation of positive surges, bores and compression waves," Environ. Fluid Mech. **16**, 695–719 (2016).

[61]F. Murzyn, D. Mouaze, and J. Chaplin, "Optical fibre probe measurements of bubbly flow in hydraulic jumps," Int. J. Multiphase Flow **31**, 141–154 (2005).

[62]H. Chanson, *Air Bubble Entrainment in Free-Surface Turbulent Shear Flows* (Elsevier, 1996).

[63]T. Brattberg, L. Toombes, and H. Chanson, "Developing air-water shear layers of two-dimensional water jets discharging into air," in American Society of Mechanical Engineers, Fluids Engineering Division (Publication) FED, 1998.

14 November 2024 05:38:19